JAEA-Research
2023-006
DOI:10.11484/jaea-research-2023-006

Optimized Phase-field Modeling Using a Modified Conservative Allen-Cahn Equation for Two-phase Flows

Kenta SUGIHARA, Naoyuki ONODERA, Yasuhiro IDOMURA and Susumu YAMASHITA

Center for Computational Science & e-Systems

October 2023

Japan Atomic Energy Agency | 日本原子力研究開発機構

JAEA-Research

本レポートは国立研究開発法人日本原子力研究開発機構が不定期に発行する成果報告書です。
本レポートの転載等の著作権利用は許可が必要です。本レポートの入手並びに成果の利用（データを含む）は、下記までお問い合わせ下さい。
なお、本レポートの全文は日本原子力研究開発機構ウェブサイト（https://www.jaea.go.jp）より発信されています。

国立研究開発法人日本原子力研究開発機構　JAEA イノベーションハブ　研究成果利活用課
〒 319-1195　茨城県那珂郡東海村大字白方 2 番地 4
電話 029-282-6387, Fax 029-282-5920, E-mail:ird-support@jaea.go.jp

This report is issued irregularly by Japan Atomic Energy Agency.
Reuse and reproduction of this report (including data) is required permission.
Availability and use of the results of this report, please contact
Institutional Repository and Utilization Section, JAEA Innovation Hub,
Japan Atomic Energy Agency.
2-4 Shirakata, Tokai-mura, Naka-gun, Ibaraki-ken 319-1195 Japan
Tel +81-29-282-6387, Fax +81-29-282-5920, E-mail:ird-support@jaea.go.jp

© Japan Atomic Energy Agency, 2023

JAEA-Research 2023-006

Optimized Phase-field Modeling Using a Modified Conservative Allen-Cahn Equation for Two-phase Flows

Kenta SUGIHARA, Naoyuki ONODERA, Yasuhiro IDOMURA

and Susumu YAMASHITA†

Center for Computational Science & e-Systems
Japan Atomic Energy Agency
Kashiwa-shi, Chiba-ken

(Received July 31, 2023)

This report presents a new surface capturing method based on the phase field model for gas-liquid two-phase flows simulation. In the conventional phase field model, the interface correction strength parameter was determined from the maximum flow velocity in the computational domain, but because the interface correction was applied uniformly to the entire space, it was also applied to locations that did not require correction. In the new method, the phase field parameter or the intensity of the phase field model is extended to have a spatial distribution, allowing us to set the optimal parameters depending on the local flow velocity fields. We also propose a method to derive the optimal phase field parameter based on systematic parameter scans using error analysis of the interface advection test and bubble rising calculations. Through benchmark tests of gas-liquid two-phase flows, the proposed model is verified, and it is shown that the proposed model has higher accuracy than the conventional phase field model.

Keywords: Phase Field Method, Conservative Allen-Cahn Equation, Modified Conservative Allen-Cahn Equation, Two-phase Flow

†Nuclear Science and Reactor Engineering Division, Nuclear Science and Engineering Center, Nuclear Science Research Institute, Sector of Nuclear Science Research

気液二相流計算における修正conservative Allen-Cahn方程式を用いたフェーズフィールド法の最適化

日本原子力研究開発機構　システム計算科学センター

杉原　健太、小野寺　直幸、井戸村　泰宏、山下　晋 †

(2023 年 7 月 31 日受理)

本報告書では、気液二相流シミュレーションのためのフェーズフィールドモデルに基づく新しい界面捕獲法を提案する。従来のフェーズフィールドモデルでは、界面補正強度パラメータは計算領域内の最大流速から決定されていたが、界面補正は空間全体に一様に適用されているため、補正を必要としない位置にも適用されていた。新手法では、フェーズフィールド変数あるいはフェーズフィールドモデルの強度に空間分布を持つように拡張し、局所的な流速場に応じた最適なパラメータを設定できるようにした。また、界面移流試験や気泡上昇計算の誤差解析を用いた系統的なパラメータスキャンに基づき、最適なフェーズフィールドパラメータを導出する手法を提案する。気液二相流のベンチマークテストを通じて、提案モデルを検証し、提案モデルが従来のフェーズフィールドモデルよりも高精度であることを示す。

システム計算科学センター：〒 277-0871　千葉県柏市若柴 178-4　柏の葉キャンパス 148 街区 4
† 原子力科学研究部門 原子力科学研究所 原子力基礎工学研究センター 核工学・炉工学ディビジョン

Contents

1 Introduction **1**

2 Modified conservative phase-field method **3**
2.1 Conservative phase-field method 3
2.2 Equilibrium profile of the conservative phase-field method 3
2.3 Modified conservative Allen-Cahn equation 4
2.4 Unit normal vector 4
2.5 Spacial distribution of γ 4
2.5.1 Cutoff filter for phase field flux 5
2.5.2 Mass-redistribution method 6

3 Verification studies **7**
3.1 1D advection test 7
3.2 3D advection test 8
3.3 Zalesak's solid rotation test 9

4 Two phase flow solver **11**
4.1 Incompressible Navier-Stokes equation 11
4.2 Velocity-pressure coupling 11
4.3 Surface tension force model 12
4.4 Numerical stability 13

5 Verification of the MCAC method **15**
5.1 Single bubble rising problem 15
5.1.1 Simulation condition 15
5.1.2 Optimal parameter for the velocity gradient term 16
5.2 Droplet oscillation problem 17

6 Concluding remark **18**

Acknowledgments **19**

References **20**

Appendix **46**

目　次

1　序論 **1**

2　修正保存型フェーズフィールド法 **3**
2.1　保存型フェーズフィールド法 3
2.2　保存型フェーズフィールド法の平衡分布 3
2.3　修正保存型 Allen-Cahn 方程式 4
2.4　単位法線ベクトル 4
2.5　γ の空間分布 4
2.5.1　フェーズフィールド流束のカットオフフィルタ 5
2.5.2　質量再分配法 6

3　検証テスト **7**
3.1　一次元移流テスト 7
3.2　三次元移流テスト 8
3.3　Zalesak の剛体回転テスト 9

4　二相流計算 **11**
4.1　非圧縮性 Navier-Stokes 方程式 11
4.2　速度と圧力のカップリング 11
4.3　表面張力モデル 12
4.4　数値安定性 13

5　MCAC 法の検証テスト **15**
5.1　単一気泡上昇問題 15
5.1.1　計算条件 15
5.1.2　速度勾配項の最適値 16
5.2　液滴振動問題 17

6　結論 **18**

謝辞 **19**

参考文献 **20**

付録 **46**

List of Tables

Table 1 Optimal values of M for various advection schemes ($\delta = 3\Delta x$) 22
Table 2 Errors and convergence rates for the Zalesak's tests. 22
Table 3 Dependency of resolution for oscillation frequency and damping rate. $\delta/\Delta x = 3.0$ 22

List of Figures

Figure 1 An equilibrium solution ϕ_{eq} is shown for the interface width $\delta = 4$ and the smoothness parameter $\lambda = 0.05$. 23
Figure 2 Conversion from the VOF function (black) to the level set function. Red shows an ideal level set function. Blue and green show level set functions converted using $\alpha = 0.001$ and $\alpha = 0.0001$, respectively. The VOF function is given by an equilibrium solution with $\delta = 4$ and $\lambda = 0.05$. 23
Figure 3 Illustration of a typical deformation velocity field for interfacial advection. . . . 24
Figure 4 An example of the spatial distribution of (a) γ, (b) velocity term, (c) compression/expansion component of velocity gradient term, and (d) shear component of velocity gradient term in a single bubble rise calculation. The cross section of case (D) in Fig. 17 are shown for $M = 0.8$, $B = 1.0$, and $\alpha = 0.0001$. 25
Figure 5 VOF functions are shown for 1D advection tests with $\Delta x = 0.01$, $\Delta t = 0.001$, $u_0 = 1$, and $\gamma = 1$. In (a), a black curve shows the initial profile given by an equilibrium solution with $\delta = 3\Delta x$ and $\lambda = 0.05$. Green, blue, and red curves show profiles after one advection period computed using the first-order FVM scheme, the third-order WENO scheme, and the fifth-order WENO scheme, respectively. (b) shows the same plot near the left interface. 26
Figure 6 u_0 scans of the interface width are conducted with $\gamma = 1$. (a) and (b) are computed using the initial equilibrium profiles with $\delta = 3\Delta x$ and $\lambda = 0.05$ and with $\delta = 4\Delta x$ and $\lambda = 0.05$, respectively. 26
Figure 7 γ scans of the interface width are conducted with $u_0 = 1$. (a) and (b) are computed using the initial equilibrium profiles with $\delta = 3\Delta x$ and $\lambda = 0.05$ and with $\delta = 4\Delta x$ and $\lambda = 0.05$, respectively. 27
Figure 8 u_0 scans of the interface width are conducted with $\gamma = u_0$. (a) and (b) are computed using the initial equilibrium profiles with $\delta = 3\Delta x$ and $\lambda = 0.05$ and with $\delta = 4\Delta x$ and $\lambda = 0.05$, respectively. 27
Figure 9 The computational domain and the initial condition of 3D advection tests. . . . 28
Figure 10 Dependence of the shape and the width of the interface on the phase field parameter γ. 28
Figure 11 Dependence of the errors on the phase field parameter $\gamma = M|\mathbf{u}|$ in 3D advection tests with $\delta = 3\Delta x$. 29
Figure 12 Dependence of the error on the interface width δ in 3D advection tests. 30

Figure 13 The initial distribution and the rotating velocity field for the Zalesak's test. . . 30
Figure 14 Contour plots of the VOF function after one rotation period. Contours at $\phi = 0.05, 0.5, 0.95$ are shown. 31
Figure 15 Staggered variable arrangement and index definition. 31
Figure 16 Limitations of time step widths in droplet oscillation and bubble rising problems. 32
Figure 17 Left shows the computational domain of the bubble rising problem. Right shows comparisons of bubble shapes between the CAC (left half) and MCAC (right half) results. The bubble shapes in four parameter regimes are characterized as (A) Spherical, (B) Ellipsoidal, (C) Skirted, and (D) Dimpled. The isosurface is shown for $\phi = 0.5$. 32
Figure 18 Evaluation area of bubble volume error (Case-C, Skirted, MCAC, $D_b/\Delta x = 32$, $B = 1$). The four contour lines are $\phi = 0.05, 0.5, 0.95$, and $\psi = 2\delta$, respectively. 33
Figure 19 Test results using the MCAC method. The bubble Reynolds number is plotted against the parameter of velocity gradient term B. Also shown are the results using the CAC method. The bubble Reynolds number Re is normalized by the experimental value Re (Grace). 34
Figure 20 Test results using the MCAC-CO method. The same definition as Fig.19 is used. 35
Figure 21 Test results using the MCAC-MR method. The same definition as Fig.19 is used. 36
Figure 22 Test results using the MCAC-COMR method. The same definition as Fig.19 is used. 37
Figure 23 Test results using the MCAC method. The bubble volume error $\int_\Omega |1-\phi| dV$ is plotted against the parameter of velocity gradient term B. Also shown are the results using the CAC method. 38
Figure 24 Test results using the MCAC-CO method. The same definition as Fig.23 is used. 39
Figure 25 Test results using the MCAC-MR method. The same definition as Fig.23 is used. 40
Figure 26 Test results using the MCAC-COMR method. The same definition as Fig.23 is used. 41
Figure 27 Comparisons of the bubble Reynolds numbers obtained using the CAC, MCAC, MCAC-CO, MCAC-MR, and MCAC-COMR methods with $M = 0.8$, $B = 1.0$, and the grid resolution of $D_b/\Delta x = 16$, 32, where D_b is the diameter of the initial spherical bubble. 42
Figure 28 Comparisons of the bubble volume error for the CAC, MCAC, MCAC-CO, MCAC-MR, and MCAC-COMR methods with $M = 0.8$, $B = 1.0$, and the grid resolution of $D_b/\Delta x = 16$, 32. 42
Figure 29 Set up for 3D water droplet oscillation simulation. 43
Figure 30 The time histories of the droplet radius in droplet oscillation tests. 44
Figure 31 Arrangement of spatial gradient variables of volume fraction for curvature calculations. 45

1 Introduction

Understanding of gas-liquid two-phase flows is important for designing cooling systems based on boiling refrigerants in various industrial fields, such as boiling water reactors [1, 2], and analysis using computational fluid dynamics (CFD) is expected to play a critical role. In analysing gas-liquid two phase flows, there are two main numerical approaches, two-fluid models and one-fluid models. Two-fluid models can describe dispersed two-phase flows, that include many fine bubbles, with lower grid resolution, while their accuracy largely depends on constitutive equations describing transfer of mass, momentum, and energy between gas and liquid phases. On the other hand, one-fluid models directly describe gas and liquid phases by capturing the gas-liquid interface. Although this approach requires costly computation to resolve each bubble, it does not rely on constitutive equations, and also, it can treat the effect of the surface tension force. With increasing computing power, the utility of the latter approach has been expanded.

The accuracy of one-fluid models depends on interface tracking/capturing methods, and so far, various methods such as the front tracking method [3], the level set method [4], the VOF/PLIC (volume of fluid/piecewise linear interface calculation) method [5], the THINC/WLIC (tangent of hyperbola for interface capturing/weighted line interface calculation) method [6], and the phase field method [7] have been proposed. The front tracking method uses Lagrangian markers to directly track the location of the interface. Although the calculation accuracy to track the interface position is high, the interface must be reconstructed to represent geometric changes such as coalescence and separation of the interface. The level set method implicitly expresses the interface position using the signed distance function (SDF) ψ, which gives the interface by $\psi = 0$. The movement of the interface is expressed by advecting the SDF. However, the fundamental property of the SDF, $|\nabla\psi| = 1$, breaks down as the calculation proceeds, and thus, re-initialization is required. Since the SDF has a spatially smooth distribution, it has excellent accuracy in calculating geometric shapes such as the curvature and normal vector of the interface. The front tracking method and the level set method are classified as the sharp interface method, in which gas and liquid phases are defined by computing the sharp interface, and thus, numerical errors of the interface position lead to violation of the mass conservation. This issue was resolved by the VOF method [8], in which the VOF function ϕ describes the gas phase with $\phi = 0$ and the liquid phase with $\phi = 1$, and the interface is given by a diffused zone with a finite width. This kind of approach is called as the diffuse interface method. In the VOF method, the mass of fluid is defined as $\rho = \phi\rho_l + (1 - \phi)\rho_g$, and its conservation is guaranteed by advecting the VOF function via conservative schemes, where ρ_g and ρ_l are the mass of gas and liquid phases, respectively. In addition, the VOF method does not require explicit tracking of interface positions, and no special treatment is required for topological changes such as coalescence or separation of interfaces. The VOF/PLIC method has high accuracy, but its interface reconstruction method is difficult to implement in three dimensional (3D) problems. The THINC/WLIC method is a VOF method, in which a hyperbolic function is used as an interpolation function to calculate advection of the interface while maintaining its width, and thus, complex interface reconstruction is not required unlike the PLIC method. Here, the original THINC method

[9] had a problem in the accuracy of interface geometry in multidimensional calculations. Yokoi applied the WLIC method to the THINC method to enable interface advection that results in smooth interface geometry even in multidimensional calculations [6].

In recent years, the VOF methods are widely used for analysing gas-liquid two-phase flows. However, in long time simulations, the conventional VOF methods often generate fragmentation of the VOF function due to numerical diffusion. This issue was resolved by the phase field method [7], which was developed based on the phase field model for interfacial problems in materials science. There are two main types of conservative phase field methods for interface tracking: the Cahn-Hilliard (CH) equation [10] and the conservative Allen-Cahn (CAC) equation [7]. Since the CH equation has the fourth-order spatial derivative, the stability condition for the time step width is limited to $\Delta t \sim O(\Delta x^4)$, where Δx is the grid width. On the other hand, as the CAC equation involves only up to the second-order spatial derivative, the stability condition is relaxed to $\Delta t \sim O(\Delta x^2)$, allowing the use of larger time intervals than in the CH equation. In this work, we address the phase field method based on the CAC equation. The CAC equation is given by a convection-diffusion equation, in which both diffusion and anti-diffusion terms are involved. Here, the anti-diffusion term can cancel errors due to numerical diffusion coming from other terms, and the calculation results naturally approach an equilibrium solution, which is given by a hyperbolic function as in the THINC method. Because of this advantage, the motion of the interface is described by the computation of the VOF function via conservative Eulerian schemes with finite numerical diffusion, and geometric reconstruction of interfaces is not needed unlike other VOF methods.

Although the phase field method is one of the promising VOF methods, it still needs to be improved regarding the following two points. The first issue is that model parameters are defined to be uniform over the entire space. In the conventional phase field method [7], the phase field parameter $\bar{\gamma}(t)$, which determines the strength of interface modification by the phase field model, was given based on the maximum fluid velocity in the entire computational domain. However, when the fluid velocity is largely different at each position, $\bar{\gamma}(t)$ chosen by the above rule may be too strong at the positions with lower velocities. If the interface modification is too strong, the interface is often deformed to align the computational grid. To resolve this issue, in this study, we propose a new phase field method, in which a new phase field parameter $\gamma(t, \mathbf{x})$ depends also on the position. To facilitate this correction, we also propose a modified conservative Allen-Cahn (MCAC) equation, which keeps a conservative form even with the spatial change of the phase field parameter. Another issue is that the phase field parameter is determined empirically. In this study, we derive the optimal phase field parameter based on comprehensive error analysis in fundamental interface advection tests and single bubble rising tests. Benchmark tests of interface advection and gas-liquid two-phase flows are performed to demonstrate the superiority of the proposed MCAC method compared to the conventional CAC method.

In Section 2, the CAC equation and it's equilibrium profile are explained, and the MCAC equation is proposed. In Section 3, an optimization method for the phase field parameter is presented. Sensitivity analysis of the phase field parameter in 1D interface advection test is performed, and the validity of the new optimization method is confirmed. The optimal phase field parameter is

derived using error analysis of 3D interface advection tests. In Section 4, the gas-liquid two-phase flow model is described. In Section 5, the water droplet oscillation and bubble rising problems are calculated using the proposed MCAC methods, and the numerical results are validated against the results of the conventional CAC method and theoretical solutions. The conclusions are summarized in Section 6.

2 Modified conservative phase-field method

In this section, the CAC equation and its equilibrium solution developed by Chiu et al. [7] are explained, and then the MCAC equation proposed in this paper is introduced.

2.1 Conservative phase-field method

The phase field variable or the VOF function ϕ in the CAC equation smoothly and steeply connects the gas phase with $\phi = 0$ to the liquid phase with $\phi = 1$ across the interface defined at $\phi = 0.5$. The governing equation is described as

$$\frac{\partial \phi}{\partial t} + \nabla \cdot (\mathbf{u}\phi) = \bar{\gamma} \left(\varepsilon \nabla \cdot (\nabla \phi) - \nabla \cdot \left(\phi(1-\phi) \frac{\nabla \phi}{|\nabla \phi|} \right) \right), \tag{1}$$

where $\mathbf{u}$ is the velocity vector describing the movement of the interface, $\bar{\gamma}$ is the phase field parameter describing the intensity of the phase field model, and ε is a constant related with the relative magnitudes of the diffusion and anti-diffusion terms in the phase field model. Here, the thickness of the interface is controlled by ε. In Ref.[7], $\bar{\gamma}(t) = |\mathbf{u}_{\max}(t)|$ and $\varepsilon = 0.7\Delta x$ were chosen, where $|\mathbf{u}_{\max}|(t)$ is the maximum velocity in the computational domain at each time step. The advection term was calculated using the dispersion-relation-preserving dual-compact upwind advection scheme [11], and the overshoot and undershoot caused by advection calculations are corrected by the mass-redistribution method.

2.2 Equilibrium profile of the conservative phase-field method

The equilibrium solution of the CAC equation is given as

$$\phi_{\mathrm{eq}} = \frac{1}{2} \left[1 + \tanh \left(\frac{\psi}{2\varepsilon} \right) \right], \tag{2}$$

where ψ is the SDF with respect to the interface at $\phi = 0.5$. ε is related to the interface width δ and the interface smoothness parameter λ as

$$\varepsilon = \frac{\delta}{2b}, \tag{3}$$

$$b = 2 \tanh^{-1}(1 - 2\lambda). \tag{4}$$

In this study, λ is fixed to 0.05, which gives $\delta = 4.12\Delta x$ with $\varepsilon = 0.7\Delta x$. Figure 1 shows the relationship between the equilibrium profile and these parameters.

2.3 Modified conservative Allen-Cahn equation

We propose the MCAC method, in which the phase-field parameter $\gamma(t, \mathbf{x})$, is not a constant, but is assumed to be spatially varied depending on the velocity field, etc. In order to facilitate this modification while keeping the conservative formulation, we propose the following equation,

$$\frac{\partial \phi}{\partial t} + \nabla \cdot (\mathbf{u}\phi) = \nabla \cdot \left(\gamma \varepsilon (\nabla \phi) - \gamma \left(\phi(1-\phi) \frac{\nabla \phi}{|\nabla \phi|} \right) \right), \tag{5}$$

where γ is moved into the divergence. It is noted that the above MCAC equation involves correction terms, compared to the original CAC equation, which is based on the Allen-Cahn equation for the interfacial problems in materials science. However, in the phase field method for CFD applications, we do not need to compute the Allen-Cahn equation, provided that the dynamics of the interface is accurately described. The accuracy of the MCAC equation will be demonstrated in the following sections.

2.4 Unit normal vector

The accuracy of the unit normal vector $\mathbf{n} = \nabla\phi/|\nabla\phi|$, which appears in the second term of the r.h.s., directly affects the accuracy of the interface geometry in the phase-field method as well as the surface tension force in the two-phase flow calculation. Smoothing methods are widely used to improve the accuracy when unit normal vectors are calculated using volume fractions. On the other hand, the level set method is a well-known approach for accurately calculating the interface profile. Since the level set function has a smoother distribution than the VOF function, this approach can calculate unit normal vectors more accurately than smoothing methods using the VOF function. In this study, unit normal vectors are re-defined as $\mathbf{n}' = \nabla\psi/|\nabla\psi|$ using the SDF $\psi(\mathbf{x})$ converted from the VOF function $\phi(\mathbf{x})$, and $\nabla\phi/|\nabla\phi|$ in Eq.(5) is replaced by $\mathbf{n}'$. It is noted that $\mathbf{n}'$ is used also in computation of the interface curvature in the surface tension force model (see Appendix).

The conversion from the VOF function to the SDF in Fig. 2 is defined as

$$\psi = \begin{cases} \varepsilon \ln \frac{\alpha}{1-\alpha} & \text{for } \phi < \alpha, \\ \varepsilon \ln \frac{\phi}{1-\phi} & \text{for } \alpha \le \phi \le 1-\alpha \ , \\ \varepsilon \ln \frac{1-\alpha}{\alpha} & \text{for } 1-\alpha < \phi, \end{cases} \tag{6}$$

where α is a small value. In this study, $\alpha = 0.0001$ is used. It can be confirmed that this choice gives the SDF over $\sim 6\Delta x$ from the interface. The phase field model and the surface tension force work only in the vicinity of the interface or over $\delta/2 \sim 2\Delta x$ from the interface. Therefore, the SDF defined for six grids from the interface is sufficient.

2.5 Spacial distribution of γ

In interface advection calculations using the diffuse interface method, there are two causes of numerical diffusion of interface. One is numerical diffusion of the interface in advection calculations, the other is a deformation of the interface due to velocity fields such as expansion and stretching.

For example, in a constant velocity field or a rigid rotation velocity field as shown in Figs. 3(a) and 3(b), deformation of the interface does not ideally occur, but numerical diffusion in advection calculations can widen the interface width. On the other hand, in Figs. 3(c) and 3(d), velocity fields show compression, expansion, and shearing, and the interface width may be changed by deformation of the interface even without numerical diffusion. When the interface width is changed by the above effects, the phase field model modifies the interface width to a constant width, so that the equilibrium solution is recovered. Here, the modification intensity depends of the phase field parameter.

The conventional phase field method uses a spatially uniform phase field parameter which is given by the maximum flow velocity in the entire computational domain, such as $\bar{\gamma} = 0.7|\mathbf{u}_{max}|$. Since the numerical viscosity in advection calculations is proportional to the advection velocity, the above choice appears reasonable. However, in gas-liquid two-phase flow calculations, the velocity can vary greatly, especially in the velocity of gas. For example, in a typical dam break problem, the maximum flow velocity can be more than an order of magnitude larger than the average flow velocity. In such a situation, using the maximum flow velocity in the entire computational domain may make the phase field model too strong, resulting in unphysical deformation of the interface shape along the grid and/or a severe numerical stability condition.

In this study, we consider a spatial change in the phase field parameter γ to avoid these issues. Firstly, we take account of the spacial distributions of the velocity and the deformation velocity tensor, which may reflect the above two effects, and write the phase field parameter as

$$\gamma(t, \mathbf{x}) = M\ |\mathbf{u}| + B\ |\mathbf{S}|\delta, \tag{7}$$

where M and B are dimensionless constants, the second term is multiplied by the interface width δ to make its dimension consistent, and $\mathbf{S}$ is the deformation velocity tensor

$$\mathbf{S} = S_{ij} = \frac{1}{2}\begin{pmatrix} 2\ u_x & u_y + v_x & u_z + w_x \\ v_x + u_y & 2\ v_y & v_z + w_y \\ w_x + u_z & w_y + v_z & 2\ w_z \end{pmatrix}. \tag{8}$$

Here, $\mathbf{S}$ is defined in the Cartesian coordinate system (x, y, z), u, v, w are the x, y, z components of the velocity vector, and the subscripts x, y, z are the derivatives in each direction. The absolute value of the deformation velocity tensor $\mathbf{S}$ is defined as

$$|\mathbf{S}| = \sqrt{S_{ij}S_{ij}} = \sqrt{S_{11}^2 + S_{12}^2 + S_{13}^2 + S_{21}^2 + S_{22}^2 + S_{23}^2 + S_{31}^2 + S_{32}^2 + S_{33}^2}. \tag{9}$$

The diagonal terms of $\mathbf{S}$ represent compression and expansion as in Fig. 3(c), while the off-diagonal terms refer to shear as in Fig. 3(d).

2.5.1 Cutoff filter for phase field flux

The above model may be calculated for the entire computational domain. However, it works only near the interface and is negligible in regions away from the interface. On the other hand, from the

numerical viewpoint, when the flow velocity becomes large in regions away from the interface, the phase field model with the second order derivative may limit the numerical stability. To avoid such a numerical issue, the phase field parameter is modified so that it works only near the interface,

$$\gamma(t,\mathbf{x}) = \begin{cases} 0 & (\phi < \alpha), \\ M\ |\mathbf{u}| + B\ |\mathbf{S}|\delta & (\alpha \le \phi \le 1-\alpha), \\ 0 & (1-\alpha < \phi). \end{cases} \tag{10}$$

The optimal value of M is determined by the discretization of the advection term, and it is optimized by a 3D advection test. On the other hand, the optimal value of B depends on a deformation of the interface induced by the effects of compression, expansion, and shearing in the flow field. In this work, we estimate the optimal value of B in a single bubble rising problem, which shows different deformations of the interface depending on flow parameter regimes.

Since the MCAC equation is discretized in a flux form on the Cartesian grid system, we calculate the velocity term (the first term) of the γ on the cell-face as

$$M\ |\mathbf{u}|_{i-\frac{1}{2},j,k} = M\sqrt{u^2_{i-\frac{1}{2},j,k} + v^2_{i-\frac{1}{2},j,k} + w^2_{i-\frac{1}{2},j,k}}\ , \tag{11}$$

where (i,j,k) are the grid indices in the (x,y,z) directions. Here, $(i-\frac{1}{2},j,k)$ means the cell-face in the "$-x$" side of the (i,j,k)-th cell. Since this study employs a staggered variable configuration and each velocity component is not defined at the same location, v and w at the cell-face in the "$-x$" side are calculated by the following equations,

$$v_{i-\frac{1}{2},j,k} = \frac{1}{4}\left(v_{i-1,j-\frac{1}{2},k} + v_{i,j-\frac{1}{2},k} + v_{i-1,j+\frac{1}{2},k} + v_{i,j+\frac{1}{2},k}\right), \tag{12}$$

$$w_{i-\frac{1}{2},j,k} = \frac{1}{4}\left(w_{i-1,j,k-\frac{1}{2}} + w_{i,j,k-\frac{1}{2}} + w_{i-1,j,k+\frac{1}{2}} + w_{i,j,k+\frac{1}{2}}\right). \tag{13}$$

The velocity components at the cell-faces in the y and z sides can be calculated in the same way. The velocity gradient term (the second term) of γ is also calculated in the same way on the cell-face using the second-order centered finite difference scheme.

An example of the spatial distribution of γ around a rising bubble is shown in Fig. 4. The distribution of the velocity term is larger at the center of the bubble as shown in Fig. 4(b) due to buoyancy. The velocity gradient term becomes large at the bubble interface, with compression at the top, expansion at the bottom, and shearing at the sides. By combining these terms and applying the filter near the interface, the resulting spatial distribution of the phase field parameter is obtained as shown in Fig. 4(a).

2.5.2 Mass-redistribution method

Even with higher-order advection schemes and/or limiters, a solution of the phase field equation may contain small undershoot/overshoot. The mass-redistribution method has been proposed to avoid such undershoot/overshoot while keeping the global conservation of mass or the VOF function [7]. The mass-redistribution procedure is given as follows.

1. Filter the undershoot/overshoot values,

$$\phi = \begin{cases} 1 & (1 + 10^{-7} < \phi) \\ 0 & (\phi < 10^{-7}) \\ \phi & (else) \end{cases} \tag{14}$$

2. Compute the current total mass,

3. Compute the difference of the total mass between the initial and present time,

4. Uniformly distribute the mass difference into the computational cells in the transition region ($0.05 < \phi < 0.95$).

3 Verification studies

In this section, we verify the velocity term of γ in the MCAC method. Firstly, we compute 1D and 3D advection tests with uniform velocity fields, and examine an impact of the numerical diffusion which depends on advection schemes and model parameters on the interface width. From these tests, we derive the optimum value of M. As the CAC and MCAC methods give almost the same results for uniform velocity fields, we show only the results from the CAC method. We then compare the CAC and MCAC methods in the Zalesak's solid rotation test, which uses non-uniform velocity fields. Here, the influence of the spatial distribution of γ can be confirmed because of the large velocity difference between the center of rotation and the periphery in the rotational velocity field. It is noted that in uniform velocity fields and in rigid rotation fields, the velocity gradient term becomes zero, and in this section, we focus only on the velocity term.

3.1 1D advection test

Figure 5 shows the results of 1D advection tests conducted using the CAC equation (1). Here, the computational domain is periodic, the normalized system size is $L = 1$, the grid width is $\Delta x = L/100$, and the normalized constant velocity is $u_0 = 1$. The initial distribution is given by a square like wave, which satisfies the equilibrium solution (2) at the interface, and it is advected for one period up to the normalized time of $t = 1$ (see Fig. 5(a)). In the CAC equation, $\gamma = 1$ and $\varepsilon = 0.51\Delta x$ ($\delta = 3\Delta x$ and $\lambda = 0.05$) are chosen. The advection term is discretized using the first-order upwind finite volume method (FVM) and the third and fifth-order weighted essentially non-oscillatory (WENO) schemes. The third-order total variation diminishing (TVD) Runge-Kutta method is used for the time integration with the time step width of $\Delta t = 0.001$. The interface width is defined as the spacial distance from $\phi = \lambda$ to $\phi = 1 - \lambda$, as in the equilibrium solution (see Fig. 1), and both upwind and downwind interface widths were measured and averaged.

In Fig. 5(b), it is confirmed that the interface width is different depending on the advection scheme, and higher order schemes give solutions closer to the equilibrium solution. It is noted that

after one period, the interface width is almost unchanged, and thus, we optimize model parameters against numerical results after one period.

In order to clarify the relation between the phase field parameter and the numerical diffusion, which is determined by the advection velocity and the advection scheme, we conduct u_0 scans at fixed γ and γ scans at fixed u_0. In Fig. 6, u_0 scans at $\gamma = 1$ clearly show an impact of the numerical diffusion on the interface width. The interface width becomes wider with larger u_0, and its increasing rate is changed depending on the advection scheme and the number of grids used to resolve the interface. In Fig. 7, γ scans at $u_0 = 1$ indicate that an influence of the numerical diffusion can suppressed by increasing the intensity of the phase field model. In all cases, the normalized interface width is converged to unity by increasing γ, while its decreasing rate is different depending on the advection scheme.

We then show u_0 scans with $\gamma = u_0$, which was employed in Ref.[7]. In Fig. 8, the interface width is kept constant in all cases, while its value is different depending on the advection scheme. These results suggests that scheme dependent parameter optimization is needed for 1D advection tests.

3.2 3D advection test

In 3D advection tests, a spherical distribution with a diameter of $D = 0.5$ is set up at the center of the computational domain (see Fig. 9), and it is advected by a spatially uniform velocity field $\mathbf{u} = (1, 1, 1)$ to evaluate the error of the distribution after one cycle. Here, the error is defined as

$$\text{Error} = \frac{\sum_{i,j,k} |\phi_{i,j,k} - \phi_{exact,i,j,k}|}{\sum_{i,j,k} \phi_{exact,i,j,k}}, \tag{15}$$

The computational domain is given by a cube with $L_x \times L_y \times L_z = 1 \times 1 \times 1$, and periodic boundaries are imposed in all directions. As the velocity field is uniform, we use the CAC equation, while the phase field parameter is chosen to be proportional to the convection velocity, $\gamma = M|\mathbf{u}|$, based on the results of 1D advection tests. Here, M is a constant characterizing the intensity of the phase field model, and is subject to parameter optimization. In the initial condition, the interface of spherical distribution is given by an equilibrium solution with $\delta = 3\Delta x$ and $\lambda = 0.05$, and in the CAC equation, ε is given by these parameters. Grid resolution is varied for $D = 16\Delta x, 32\Delta x, 64\Delta x$, and $128\Delta x$, and the time step width is determined by the CFL number of 0.05. In 3D advection tests, we compare four advection schemes, the third-, fifth-, and seventh-order WENO schemes, and the third-order MUSCL scheme.

Figure 11 shows M scans for these advection schemes. All results show the existence of optimum values of M, where the error becomes minimum. This feature is qualitatively different from 1D advection tests, which showed monotonic convergence toward equilibrium solutions with increasing γ. The optimum value is determined by a competition between two causes of the error. One is the numerical diffusion due to the advection scheme. This effect was already confirmed in 1D advection tests. The other is the interface deformation due to the phase field model. This effect does not exist in 1D advection tests, because of the geometrical restriction in 1D problems, and is unique

to 2D and 3D problems. In multi-dimensional problems, too large γ makes the interface aligned to the computational grid. This is attributed to computation of the CAC equation in a conservative form via FVM type schemes, in which stencils are extended along the (x, y, z) directions. Figure 10 shows examples of solutions in 3D advection tests. When γ is too small, the interface diffuses (see Fig. 10(a)). On the other hand, when γ is too large, the interface tends to be aligned to the Cartesian grids, and the interface shape is deformed from spherical to cubic (see Fig. 10(c)). In the optimum solution, these errors are suppressed to keep both the shape and the width of the interface (see Fig. 10(b)).

In Fig. 11(a), the third-order WENO scheme shows different optimum values for $M = 0.9 \sim 1.5$ depending on the grid resolution. On the other hand, in the fifth-order WENO scheme (Fig. 11(b)), the seventh-order WENO scheme (Fig. 11(c)), and the third-order MUSCL scheme (Fig. 11(d)), the optimum value of M is independent of the grid resolution, and depends only on the advection scheme. The optimum values of M for each advection scheme are summarized in Table 1. This feature is of critical importance, because in reality, there exists multiple bubbles with different $D/\Delta x$. If the optimum value of M depends of $D/\Delta x$, one cannot choose the optimum intensity of the phase field model. Therefore, the use of higher order advection schemes is essential for the phase field method.

We then examine the dependence of the optimal M on the interface width δ. Figure 12 shows 3D advection tests with the fifth-order WENO scheme and the third-order MUSCL scheme. In these tests, the grid resolution is fixed at $D/\Delta x = 64$ and the interface width is varied for $\delta = 2.5\Delta x \sim 4.0\Delta x$. As it may be expected, the narrower interface width gives the larger numerical diffusion, leading to the larger optimal values for M.

3.3 Zalesak's solid rotation test

The Zalesak's test problem[12] is widely used to verify the accuracy of interface capturing methods. A circular profile with a diameter of 0.3 and with a blank in the region over $0.475 < x < 0.525$ and $y < 0.85$ is set up in the computational domain with $L_x \times L_y = 1 \times 1$, and is rotated with a velocity field, $\mathbf{u}(\mathbf{x}) = (y - 1/2, -(x - 1/2))$, as shown in Fig. 13. As the velocity field is non-uniform, it may be difficult to optimize the phase field parameter of the CAC equation. In this test, we compare the CAC equation with $\bar{\gamma} = M|\mathbf{u}_{max}|$ and the MCAC equation with $\gamma = M|\mathbf{u}(\mathbf{x})|$, where the fifth-order WENO scheme is used and the phase field parameter is chosen as $M = 0.8$. In the MCAC method, we apply the cutoff filter and the velocity gradient parameter is given as $B = 1.0$. In the initial condition, the interface is given by an equilibrium solution with $\delta = 3\Delta x$ and $\lambda = 0.05$, and in the CAC and MCAC equations, ε is given by these parameters. Grid resolution is varied for $L_x/\Delta x \times L_y/\Delta_y = 100 \times 100, 200 \times 200$, and 400×400, where the time step width is chosen as $\Delta t = 0.00141, 0.00070$, and 0.00035.

Figure 14 shows the contour plots of the VOF function after one rotation period $T = 2\pi$. As the magnitude of the velocity becomes $|\mathbf{u}| = \sqrt{(x - 1/2)^2 + (y - 1/2)^2}$, the phase field parameter in the CAC equation is overestimated from its optimum value, resulting in excessive modification of the

interface by the phase field model in regions with small velocity. Accordingly, the MCAC equation, which can employ the optimal values everywhere, gives better results than the CAC equation. The convergence of the Zalesak's tests is confirmed by estimating the error, Eq.(15), and the results are summarized in Table 2. The errors of the MCAC equation is 31-37% smaller than those of the CAC equation, while the rate of convergence is about first-order for both models.

4 Two phase flow solver

This section describes the details of gas-liquid two-phase flow calculation models implemented in this study.

4.1 Incompressible Navier-Stokes equation

In this study, gas-liquid two-phase flows are calculated using the incompressible Navier-Stokes equations,

$$\nabla \cdot \mathbf{u} = 0, \tag{16}$$

$$\frac{\partial \mathbf{u}}{\partial t} + (\mathbf{u} \cdot \nabla)\mathbf{u} = \frac{1}{\rho}\nabla \cdot (\mu(\nabla \mathbf{u} + (\nabla \mathbf{u})^T)) - \frac{1}{\rho}\nabla p + \frac{1}{\rho}\mathbf{F}, \tag{17}$$

where $\mathbf{u}$ is the velocity, ρ is the density, μ is the viscosity, p is the pressure, $\mathbf{F}$ is the external force including the gravitational force and the surface tension force ($\mathbf{F} = \rho\mathbf{g} + \mathbf{F}_s$).

The VOF function, which is computed using the interface tracking method, is used not only for identifying the interface but also for defining the physical properties of gas-liquid two-phase flows. In this study, the VOF function ϕ is computed using the MCAC equation (5), and the density and the viscosity are defined as

$$\rho = \rho_l \phi + \rho_g (1 - \phi), \tag{18}$$

$$\mu = \mu_l \phi + \mu_g (1 - \phi), \tag{19}$$

where ρ_l, ρ_g are the density of liquid and gas phases, and μ_l, μ_g are the viscosity of liquid and gas phases, respectively.

4.2 Velocity-pressure coupling

To improve the stability of incompressible fluid calculations, the velocity-pressure coupling model is defined using scalar quantities at the cell center and each directional component of vector quantities at the cell-face as shown in Fig. 15. The SMAC method [13] is applied to correct the velocity and the pressure for incompressible fluid calculations. The time integration procedures for the Navier-Stokes equations are given as follows: firstly, the equation of motion is computed to calculate the temporal velocity $\mathbf{u}^*$ as

$$\mathbf{u}^* = \mathbf{u}^n + \left(-(\mathbf{u}^n \cdot \nabla)\mathbf{u}^n + \frac{1}{\rho^n}\nabla \cdot (\mu^n(\nabla \mathbf{u}^n + (\nabla \mathbf{u}^n)^T)) - \frac{1}{\rho^n}\nabla p^n + \mathbf{F}^n \right) \Delta t, \tag{20}$$

and then, the modified pressure δp is computed by substituting the divergence of $\mathbf{u}^*$ into the source term of the pressure Poisson equation. Here, the superscript n means the value at the n-th time step, and $*$ means the value at the intermediate time step between n and $n+1$. To make the velocity field at the $n+1$-th step divergence free, Eq.(5) is calculated using $\mathbf{u}^n$ and the density is updated to the $n+1$-th steps before calculating the pressure Poisson equation.

$$\nabla \cdot \left(\frac{1}{\rho^{n+1}} \nabla \delta p \right) = \frac{\nabla \cdot \mathbf{u}^*}{\Delta t}. \tag{21}$$

The pressure Poisson equation is the most costly part of incompressible fluid calculations, especially for gas-liquid two-phase fluid calculations with large density contrasts, which lead to ill-conditioned matrices. A multi-grid preconditioned conjugate gradient (MG-CG) method [14] is applied to solve the pressure Poisson equation.

The modified pressure δp obtained by solving the pressure Poisson equation is used to correct the velocity as

$$\mathbf{u}^{n+1} = \mathbf{u}^* - \frac{1}{\rho^{n+1}} \nabla \delta p \ \Delta t, \tag{22}$$

and the pressure value is also updated as

$$p^{n+1} = p^n + \delta p. \tag{23}$$

In this study, the third-order TVD Runge-Kutta method [15] is applied to the time integration for Eqs. (5) and (20), where the fifth-order WENO scheme is used for the advection term, and the second-order centered finite difference scheme is employed for other terms.

4.3 Surface tension force model

The surface tension force $\mathbf{F}_s$, which is included in the external force term of the Navier-Stokes equation, is calculated by the surface tension coefficient σ, the interface curvature κ, and the unit normal vector $\mathbf{n}$ of the interface,

$$\mathbf{F}_s = -\sigma \kappa \mathbf{n}. \tag{24}$$

The surface tension force works only on the gas-liquid interface. However, it is difficult to define and compute the surface tension force on a sharp interface using Eulerian methods on the Cartesian grid system. Therefore, we adopt the continuum surface force (CSF) model [16], which calculates the surface tension force on a diffused interface as a volume force in the direction normal to the gas-liquid interface.

$$\mathbf{F}_s^{CSF} = \sigma \kappa \mathbf{n} \delta_\alpha \tag{25}$$

where κ is computed using the normal vector $\mathbf{n}'$ defined using the SDF (see Appendix), and a smoothed delta function δ_α is defined as $\mathbf{n}\delta_\alpha := \nabla \phi$.

In this study, we employ the density-scaled model based on the balanced forcing algorithm [17]. The conventional CSF models were suffering from a gas-phase shift due to the surface tension-derived acceleration in the direction normal to the gas-liquid interface, whereas the density-scaled model keeps symmetry of acceleration between the gas and liquid sides of the interface. The density-scaled model is given as

$$\mathbf{F}_{s,f}^{DS} = \frac{\rho_f}{(\rho_l + \rho_g)/2} \sigma \kappa_f (\nabla \phi)_f, \tag{26}$$

where the subscript f means the value defined at the cell-face. In the balanced forcing algorithm, the discretization for the pressure gradient ∇p is chosen to be the same as that for $(\nabla \phi)_f$, so that the surface tension force is balanced with the pressure gradient. For example, both ϕ and p are defined at the cell-center, and the x components of the surface tension force and the pressure

gradient at the cell-face in the "$-x$" side are respectively calculated using the second-order centered finite difference scheme as

$$F^{DS}_{s,x,i-1/2,j,k} = \frac{(\rho_{i,j,k}+\rho_{i-1,j,k})/2}{(\rho_l+\rho_g)/2}\sigma\kappa_{i-1/2,j,k}\frac{\phi_{i,j,k}-\phi_{i-1,j,k}}{\Delta x}, \tag{27}$$

$$(\nabla p)_{x,i-1/2,j,k} = \frac{p_{i,j,k}-p_{i-1,j,k}}{\Delta x}. \tag{28}$$

4.4 Numerical stability

In this study, all equations except the pressure Poisson equation are computed explicitly, and the time step width for the explicit time integration is subject to numerical stability conditions determined by various effects in Eqs. (5) and (17). The current gas-liquid two-phase flow model has four different limitations on the time step width: the advection and viscosity terms in the Navier-Stokes equation (17), capillary waves from the surface tension term (24), and the diffusion term in the MCAC equation (5), which can be defined as follows

$$\Delta t_{\rm adv} = C_{\rm adv}\frac{\Delta x}{|\mathbf{u}_{max}|}, \tag{29}$$

$$\Delta t_{\rm visc} = C_{\rm visc}\frac{\Delta x^2}{\nu}, \tag{30}$$

$$\Delta t_{\rm sf} = C_{\rm sf}\left(\frac{(\rho_l+\rho_g)/2}{2\pi\sigma}\right)^{\frac{1}{2}}\Delta x^{\frac{3}{2}}, \tag{31}$$

$$\Delta t_{\rm pf} = C_{\rm pf}\frac{\Delta x^2}{\gamma\varepsilon} = C_{\rm pf}\frac{2b}{\gamma(\delta/\Delta x)}\Delta x, \tag{32}$$

where $C_{\rm adv}$, $C_{\rm visc}$, $C_{\rm sf}$ and $C_{\rm pf}$ are non-dimensional constants determined by the following stability conditions. The Courant-Friedrichs-Lewy (CFL) condition limits $C_{\rm adv} < 1$. Here, $\Delta t_{\rm adv}$ depends on $\mathbf{u}_{max}$, and varies in time. Von Neumann's stability analysis gives $C_{\rm visc} < 0.5$. The CFL condition for the propagation of surface tension (capillary) waves gives $C_{\rm sf} < 1$ [16]. The stability condition for the phase field model was confirmed to be $C_{\rm pf} < 0.78$ by 1D numerical experiments. Since δ is the interface width proportional to Δx, $\delta/\Delta x$ is constant, leading to $\Delta t_{\rm pf} \propto \Delta x$.

Depending on the magnitude of the velocity, the viscosity, the surface tension coefficient, and the phase field parameters, the stability condition is determined by different effects. In addition, the stability condition for actual gas-liquid two-phase flow calculations depend also on other effects such as the flow velocity distribution and convergence of the pressure Poisson equation, and thus, may not completely match the above stability conditions. In this study, the constants of $C_{\rm adv} = 0.05$, $C_{\rm visc} = 0.1$, $C_{\rm sf} = 0.5$ and $C_{\rm pf} = 0.1$ are used, and the smallest time step width among four conditions,

$$\Delta t = \min(\Delta t_{\rm adv}, \Delta t_{\rm visc}, \Delta t_{\rm sf}, \Delta t_{\rm pf}), \tag{33}$$

is applied to the simulation. The above constants are empirically adopted based on simulations of violent flows such as dam breaking and droplet impact problems, and thus, are rather conservative choices for droplet oscillation and bubble rising problems in this study.

Figure 16 shows limitations on the time step widths for the droplet oscillation and bubble rising simulations in the next section. In these simulations, the representative flow velocities are given as 0.1m/s and 0.17m/s, respectively, which are reflected to the difference of Δt_{adv}. The stability of the droplet oscillation simulation is dominated by the surface tension force at lower resolution and by the viscosity at higher resolution. On the other hand, the stability of the bubble rising simulation is dominated by the viscosity.

5 Verification of the MCAC method

In this section, the accuracy of the MCAC method is verified by computing incompressible gas-liquid two-phase flows. Unless otherwise noted, $\delta = 3\Delta x$, $\lambda = 0.05$, $\alpha = 0.0001$, $M = 0.8$, and $B = 1.0$. Here, $M = 0.8$ is the optimal parameter commonly used for both the CAC and MCAC equations, while $B = 1.0$ in the MCAC equation is the optimal parameter derived from a single bubble rising problem in Sec. 5.1.2. The flux cutoff for the phase field equation is applied for the MCAC method. We compare the CAC and MCAC methods in bubble rising and droplet oscillation problems. The effects of flux cutoff and mass-redistribution on bubble rising velocity and bubble detachment will also be investigated in the single bubble rising problem.

5.1 Single bubble rising problem

The bubble rising problem is suitable for examining the validity of surface tension and buoyancy in gas-liquid two phase flow calculations, and has been studied experimentally and numerically. We investigate a 3D single bubble rising problem in four typical parameter regimes, and compare the obtained results with the experimental results in Ref. [18] and the simulation results in Ref. [19].

5.1.1 Simulation condition

Here, the four parameter regimes are characterized by the Molton number $Mo = \frac{g\mu_l^4(\rho_l-\rho_g)}{\rho_l^2\sigma^3}$ and the Eötvös number $Eo = \frac{g(\rho_l-\rho_g)D_b^2}{\sigma}$ as,

(A) Spherical: $Mo = 1.26 \times 10^{-3}$, $Eo = 0.971$,

(B) Ellipsoidal: $Mo = 0.100, Eo = 9.71$,

(C) Skirted: $Mo = 0.971, Eo = 97.1$,

(D) Dimpled: $Mo = 1000, Eo = 97.1$.

In these calculations, the density ratio $\rho_l/\rho_g = 100$, the viscosity ratio $\mu_l/\mu_g = 100$, the gravitational acceleration $g = 9.8\mathrm{m/s}^2$, and the diameter of the initial spherical bubble $D_b = 0.01\mathrm{m}$ are used, as in Ref. [19]. As shown in Fig. 17 (left), the initial spherical bubble is at the bottom center of the computational domain with $L_x \times L_y \times L_z = 0.04\mathrm{m} \times 0.04\mathrm{m} \times 0.12\mathrm{m}$, and the grid resolution is chosen as $D_b/\Delta x = 16$, 32.

The bubble shapes obtained by these four calculations are shown in Fig. 17 (right). The bubble shapes are similar between the MCAC and CAC results, while in case C, the MCAC result shows a smoother bubble edge shape.

In order to evaluate the quantitative accuracy, we compute the errors of the bubble Reynolds number and the bubble volume error. The former error is an important measure in the bubble rising problem, and it depends mainly on the bubble shape. The bubble Reynolds number is defined as

$$Re = \frac{\rho_l D_b V_t}{\mu_l}, \tag{34}$$

where V_t is the terminal bubble rising velocity. On the other hand, the latter error is produced by fragmentation and separation of the VOF function from stretched or expanded interface regions. To quantitatively evaluate the VOF detachment from the bubble, the bubble volume error is defined by the L1 error of the VOF function in the liquid phase region, $VolumeError = \int_\Omega |1-\phi| dV$, where the inspected region Ω is defined for $\psi > 2\delta$ away from the gas-liquid interface (see Fig. 18).

5.1.2 Optimal parameter for the velocity gradient term

The buoyancy force acting on the bubble depends on the density distribution, and the higher velocity of the gas phase inside the bubble causes a large velocity gradient near the bubble interface. As a result, a compressive velocity field is produced on the upper surface of the bubble, while an expansive velocity field is formed on the lower surface, which causes the gas-liquid interface to diffuse easily at the bottom of the bubble (see Fig. 4). To evaluate an impact of the velocity gradient term on the accuracy, B scan is performed for bubble rising calculations and the errors of the bubble Reynolds number and the bubble detachment are investigated.

The MCAC method is implemented with and without the cutoff filter (Sec.2.5.1) and the mass-redistribution (Sec.2.5.2). We classify the MCAC method into the following four implementations.

MCAC Without both the cutoff filter and the mass-redistribution,

MCAC-CO With the cutoff filter and without the mass-redistribution,

MCAC-MR Without the cutoff filter and with the mass-redistribution,

MCAC-COMR With both the cutoff filter and the mass-redistribution.

Figures 19, 20, 21, and 22 show the dependence of the bubble Reynolds number on the velocity gradient parameter B for the MCAC, MCAC-CO, MCAC-MR, and MCAC-COMR methods, respectively. Compared with the CAC method, the MCAC method shows slightly better results in the cases of the spherical bubble (case A) and the dimpled bubble (case D), and almost the same results in the cases of the ellipsoidal bubble (case B) and the skirted bubble (case C). This tendency is common also for other three methods. However, the cut-off filter slightly increases the bubble Reynolds number in case A, while the mass-redistribution reduces the bubble Reynolds number in all four cases. Depending on the competition of these two effects, the resulting accuracy becomes slightly better and worse from the MCAC method.

Figures 23, 24, 25, and 26 show the dependence of the bubble volume error on the velocity gradient parameter B for the MCAC, MCAC-CO, MCAC-MR, and MCAC-COMR methods, respectively. The MCAC methods commonly show lower errors than the CAC method for cases A, B, and D. However, case C with $D_b = 16dx$ shows different behavior for each method. The MCAC and MCAC-CO methods show lower errors than the CAC method for $0.8 \leq B \leq 2.0$. On the other hand, the MCAC-MR and MCAC-COMR methods show larger errors that the CAC method, while the mass-redistribution gives lower errors in cases A and D.

Figures 27 and 28 respectively show comparisons of the bubble Reynolds number and the bubble volume error obtained using the CAC, MCAC, MCAC-CO, MCAC-MR, and MCAC-COMR methods with $M = 0.8$ and $B = 1.0$. Here, we choose $B = 1.0$ as the optimal parameter from the above parameter scans. All methods show reasonable agreements with the experimental results, and higher resolution cases show better agreements. Compared with the CAC results, the MCAC results show slightly better results. Although an impact of the cutoff filter is not clear, the mass-redistribution significantly reduces the bubble volume error in cases A, B, and D. However, it is noted that in case C, the accuracy of the mass-redistribution is sensitive to the velocity gradient parameter B, and thus, the use of mass-redistribution may be difficult for practical applications.

5.2 Droplet oscillation problem

A droplet oscillation problem is a standard benchmark test for the gas-liquid two-phase flow [20, 17]. Aalilija et al. [21] derived theoretical solutions for 2D and 3D viscous liquid droplet oscillations. Various modes of droplet oscillations were simulated for liquid metallic droplets and the time histories of the oscillation amplitudes were compared with the theoretical solutions. The results of the 2D calculations showed very good quantitative agreements with the theoretical solutions, but the 3D calculations showed larger damping rates due to insufficient resolution. In this work, we verify the performance of the proposed methods by comparing 3D water droplet oscillation simulations with the CAC and MCAC methods against Aalilija's theoretical solutions.

The water droplet with the volume of $\frac{4}{3}\pi R_0^3$ with $R_0 = 1$mm is placed in air with zero gravitational acceleration, where the computational domain is given by a cube with $L_x \times L_y \times L_z =$ 4mm $\times$ 4mm $\times$ 4mm as shown in Fig. 29. The initial droplet shape is given by an spheroid with a disturbance $\epsilon = 0.08$, where the radii in the x direction and in the y, z directions are respectively chosen as $R_0/\sqrt{1+\epsilon}$ and $R_0(1+\epsilon)$, so that the volume becomes $\frac{4}{3}\pi R_0^3$. As the spheroid shape is dominated by $n = 2$ mode, we compare the numerical results against Aalilija's theoretical solution for the spheroid oscillation (mode $n = 2$),

$$R(\theta, t) = R_0 \left(1 + \epsilon_2(t) P_2(\cos(\theta)) - \frac{1}{5}\epsilon_2^2(t).\right), \tag{35}$$

$$\epsilon_2(t) = \epsilon \exp(-\lambda_2 t) \cos(\omega_{2,0} t). \tag{36}$$

Here, $P_2(x) = \frac{1}{2}(3x^2 - 1)$ is the second-order Legendre polynomial, θ is the angle with respect to the major axis (x-axis), and the frequency and the damping rate of the spheroid oscillation with $n = 2$ are respectively given as

$$\omega_{2,0} = \sqrt{\frac{8\sigma}{\rho_l R_0^3}}, \tag{37}$$

$$\lambda_2 = \frac{5\mu_l}{\rho_l R_0^2}, \tag{38}$$

where ρ_l, μ_l, and σ are the density, the viscosity, and the surface tension coefficient of the liquid, respectively. In this study, we evaluate the droplet radius in the x direction, and compare it against

the theoretical solution at $\theta = 0$. All oscillation data analyses are performed using the Python libraries (LMFIT and SciPy), where the oscillation frequency ω is estimated by fitting the oscillation data using a fitting function, $R(t) = R_0\left(1 + \hat{\epsilon}(t) - \frac{1}{5}\hat{\epsilon}(t)^2\right) + c$, $\hat{\epsilon}(t) = \epsilon_0 \exp(-\beta t)\cos(\omega t + \theta_0)$. On the other hand, the damping rate β is obtained by extracting the maximum point of the oscillation data, plotting it on a logarithmic scale, and fitting it using a linear function.

In Fig. 30, the oscillation data obtained using the CAC and MCAC methods are compared against the theoretical solution. Here, we apply only the cutoff filter in the MCAC method, and the velocity gradient parameter is varied as $B = 0.0, 1.0$. Although these results are converged to the theoretical solution as the resolution becomes higher, they show different damping rates at lower resolution. Table 3 shows the dependency of the frequency and the damping rate on the grid resolution. Comparisons of the CAC and MCAC results show no significant difference in the frequency, while the damping rate in the CAC is much greater than that in the MCAC result at lower resolution. In the CAC method, the phase field parameters given by $|\mathbf{u}_{max}|$ are uniform within the entire interface region, and the phase field parameter becomes too strong in regions where the velocity of the interface is smaller than $|\mathbf{u}_{max}|$. This may lead to different interface deformations between the MCAC method and the CAC method, leading to larger damping rates. The MCAC method using only the velocity term ($B = 0$) gives the best results, while the MCAC method with $B = 1.0$ also overestimates the damping rate at lower resolution. This indicates that variation of the phase field parameter depending on the velocity field in the interface region is important for reproducing the damping rate. However, the use of the velocity gradient term does not improve the accuracy of the MCAC method in this case.

6 Concluding remark

The MCAC equation was proposed as an interface capturing method for incompressible two-phase flow calculations. In this model, the CAC equation [7], in which the phase field parameter $\bar{\gamma} = |\mathbf{u}_{max}|$ was uniform and overestimated, was extended to allow the use of the optimized phase field parameter depending on the local velocity and velocity gradient field $\gamma(\mathbf{x}) = M|\mathbf{u}| + B|\mathbf{S}|\delta$. Basic verification tests in uniform velocity fields showed that γ proportional to the local velocity is appropriate for the phase field model, and the optimal value of the velocity term constant $M = 0.8$ was derived. On the other hand, when the interface deformation is induced by the effects of compression, expansion, and shearing in the flow fields, as in the bubble rising problem, the velocity gradient term also becomes important. In the single bubble rising problem, it was shown that in most flow parameter regimes, the velocity gradient parameter of $B = 1.0$ was optimal. However, in the droplet oscillation problem, the velocity gradient term lead to the overestimation of the damping rate, and the better results were obtained with $B = 0.0$. Therefore, a careful choice of the velocity gradient parameter is needed in using the MCAC method.

Acknowledgments

This research was partly supported by JSPS KAKENHI, Grant-in-Aid for Scientific Research (C) JP21K11911, and Joint Usage/Research Center for Interdisciplinary Large-scale Information Infrastructures in Japan (Project ID: jh230031). Numerical computation in this work was partially carried out on the supercomputer HPE SGI8600 at the Japan Atomic Energy Agency, and TSUBAME3.0 at the Tokyo Institute of Technology.

References

[1] S. Yamashita, T. Ina, Y. Idomura, and H. Yoshida. A numerical simulation method for molten material behavior in nuclear reactors. *Nuclear Engineering and Design*, Vol. 322, pp. 301–312, 2017.

[2] A. Ono, S. Yamashita, T. Suzuki, and H. Yoshida. Numerical simulation of two-phase flow in 4x4 simulated bundle. *Mechanical Engineering Journal*, Vol. 7, No. 3, pp. 19–00583–19–00583, 2020.

[3] S.O.Unverdi and G.Tryggvason. A Front-Tracking Method for Viscous , Incompressible , Multi-fluid Flows. *Journal of Computational Physics*, Vol. 100, pp. 25–37, 1992.

[4] M. Sussman, P. Smereka, and S. Osher. A Level Set Approach for Computing Solutions to Incompressible Two-Phase Flow. *Journal of Computational Physics*, Vol. 114, No. 1, pp. 146–159, 1994.

[5] D. Youngs. Time-Dependent Multi-Material Flow with Large Fluid Distortion. *Numerical Methods for Fluid Dynamics*, 1982.

[6] K. Yokoi. Efficient implementation of THINC scheme: A simple and practical smoothed VOF algorithm. *Journal of Computational Physics*, Vol. 226, No. 2, pp. 1985–2002, 2007.

[7] P. H. Chiu and Y. T. Lin. A conservative phase field method for solving incompressible two-phase flows. *Journal of Computational Physics*, Vol. 230, No. 1, pp. 185–204, 2011.

[8] C. W. Hirt and B. D. Nichols. Volume of fluid (VOF) method for the dynamics of free boundaries. *Journal of Computational Physics*, Vol. 39, No. 1, pp. 201–225, 1981.

[9] F. Xiao, Y. Honma, and T. Kono. A simple algebraic interface capturing scheme using hyperbolic tangent function. *International Journal for Numerical Methods in Fluids*, Vol. 48, No. 9, pp. 1023–1040, 2005.

[10] J. W. Cahn and J. E. Hilliard. Free Energy of a Nonuniform System. I. Interfacial Free Energy. *The Journal of Chemical Physics*, Vol. 28, No. 2, pp. 258–267, 1958.

[11] P. H. Chiu and T. W. H. Sheu. On the development of a dispersion-relation-preserving dual-compact upwind scheme for convection – diffusion equation. *Journal of Computational Physics*, Vol. 228, No. 10, pp. 3640–3655, 2009.

[12] S. T. Zalesak. Fully Multidimensional Flux-Corrected Transport Algorithms for Fluids. *Journal of Computational Physics*, Vol. 31, pp. 335–362, 1979.

[13] A. A. Amsden and F. H. Harlow. A simplified MAC technique for incompressible fluid flow calculations. *Journal of Computational Physics*, Vol. 6, No. 2, pp. 322–325, 1970.

[14] N. Onodera, Y. Idomura, Y. Hasegawa, S. Yamashita, T. Shimokawabe, and T. Aoki. GPU Acceleration of Multigrid Preconditioned Conjugate Gradient Solver on Block-Structured Cartesian Grid. In *The International Conference on High Performance Computing in Asia-Pacific Region*, HPC Asia 2021, pp. 120–128, New York, NY, USA, 2021. Association for Computing Machinery.

[15] S. Gottlieb and C. W. Shu. Total variation diminishing Runge-Kutta schemes. *Mathematics of Computation*, Vol. 67, No. 221, pp. 73–85, 1998.

[16] D. J.U.Brackbill and C.Zemach. A Continuum Method for Modeling Surface Tension. *Journal of Computational Physics*, Vol. 100, No. 2, pp. 335–354, 1992.

[17] M. M. Francois, S. J. Cummins, E. D. Dendy, D. B. Kothe, J. M. Sicilian, and M. W. Williams. A balanced-force algorithm for continuous and sharp interfacial surface tension models within a volume tracking framework. *Journal of Computational Physics*, Vol. 213, pp. 141–173, 2006.

[18] J.R.Grace. Shapes and Velocities of Bubbles Rising in Infinite Liquids. *Transactions of the Institution of Chemical Engineers*, Vol. 51, pp. 116–120, 1973.

[19] M. Van Sint Annaland, N. G. Deen, and J. A. Kuipers. Numerical simulation of gas bubbles behaviour using a three-dimensional volume of fluid method. *Chemical Engineering Science*, Vol. 60, No. 11, pp. 2999–3011, 2005.

[20] D. J. Torres and J. U. Brackbill. The Point-Set Method: Front-Tracking without Connectivity. *Journal of Computational Physics*, Vol. 165, No. 2, pp. 620–644, 2000.

[21] A. Aalilija, C. A. Gandin, and E. Hachem. On the analytical and numerical simulation of an oscillating drop in zero-gravity. *Computers and Fluids*, Vol. 197, pp. 1–24, 2020.

[22] K. Yokoi. A practical numerical framework for free surface flows based on CLSVOF method, multi-moment methods and density-scaled CSF model : Numerical simulations of droplet splashing. *Journal of Computational Physics*, Vol. 232, No. 1, pp. 252–271, 2013.

[23] D. P. Garrick, M. Owkes, and J. D. Regele. A finite-volume HLLC-based scheme for compressible interfacial flows with surface tension. *Journal of Computational Physics*, Vol. 339, pp. 46–67, 2017.

Table 1: Optimal values of M for various advection schemes ($\delta = 3\Delta x$)

Discretization	Number of stencils in each dimension	Optimum M
3rd-order WENO	5	0.9-1.5
5th-order WENO	7	0.8
7th-order WENO	9	0.3
3rd-order MUSCL	5	0.4-0.5

Table 2: Errors and convergence rates for the Zalesak's tests.

Mesh size(Δx)	1/100	Rate	1/200	Rate	1/400
MCAC(present)	3.84×10^{-2}	1.02	1.89×10^{-2}	1.04	9.16×10^{-3}
CAC	6.18×10^{-2}	1.16	2.75×10^{-2}	0.98	1.38×10^{-2}

Table 3: Dependency of resolution for oscillation frequency and damping rate. $\delta/\Delta x = 3.0$

	Frequency [rad/s]			Damping rate [s^{-1}]		
$D/\Delta x$	32	64	128	32	64	128
MCAC(B=0)	744.05	754.54	757.32	7.9489	3.9618	5.6278
MCAC(B=1)	748.67	754.99	757.44	13.6817	13.3851	6.0231
CAC	746.63	755.26	756.19	25.2086	19.8398	8.1323
Theoretical solution		764.37			5.0215	

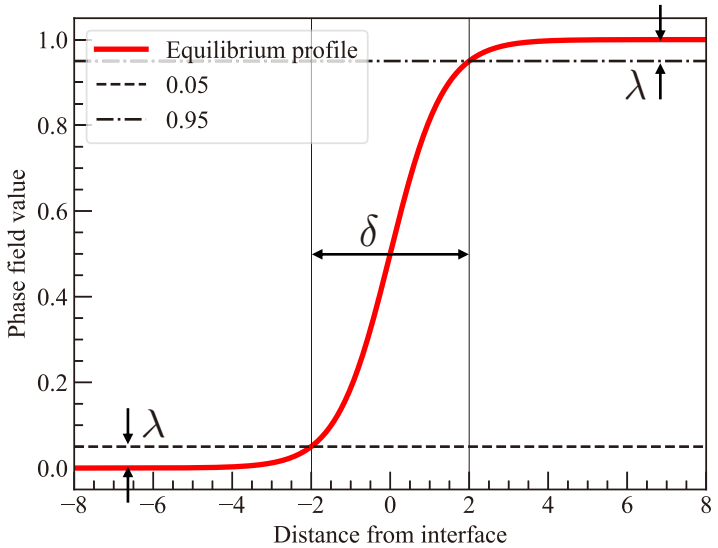

Figure 1: An equilibrium solution ϕ_{eq} is shown for the interface width $\delta = 4$ and the smoothness parameter $\lambda = 0.05$.

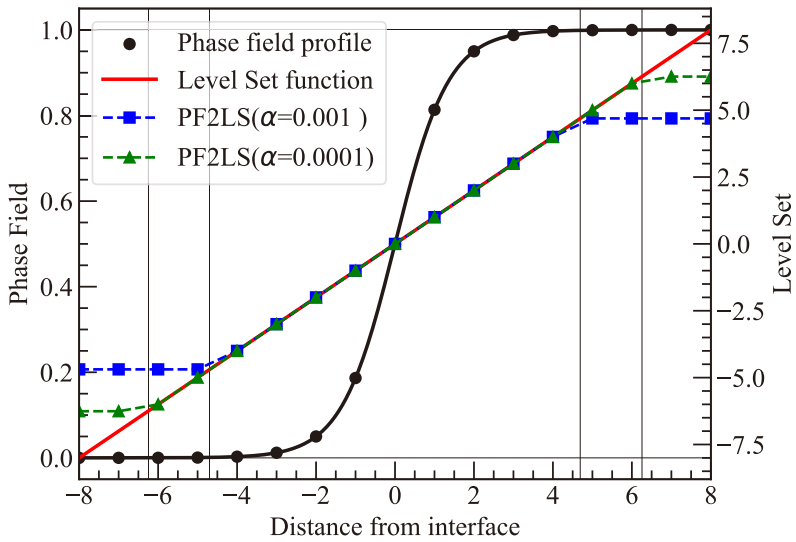

Figure 2: Conversion from the VOF function (black) to the level set function. Red shows an ideal level set function. Blue and green show level set functions converted using $\alpha = 0.001$ and $\alpha = 0.0001$, respectively. The VOF function is given by an equilibrium solution with $\delta = 4$ and $\lambda = 0.05$.

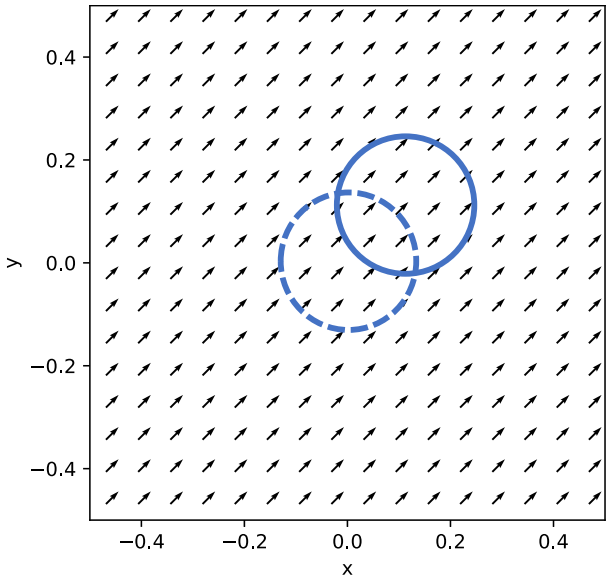

(a) Translation

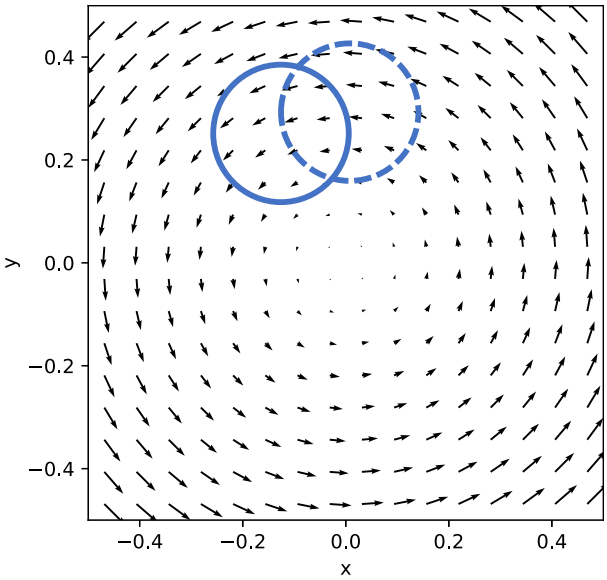

(b) Solid rotation

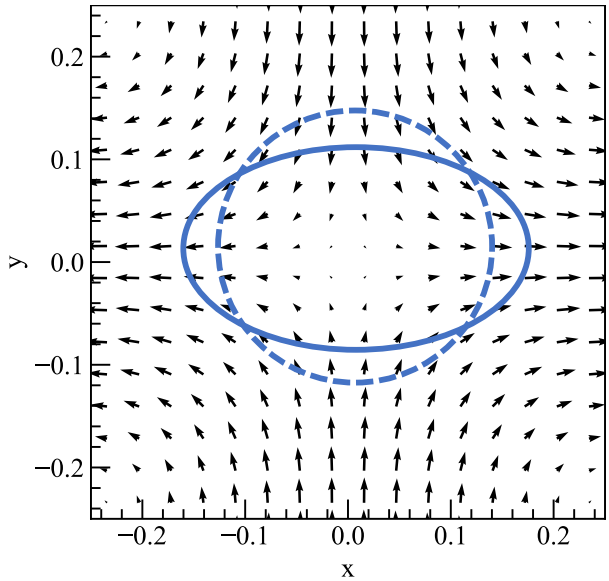

(c) Compression and expansion

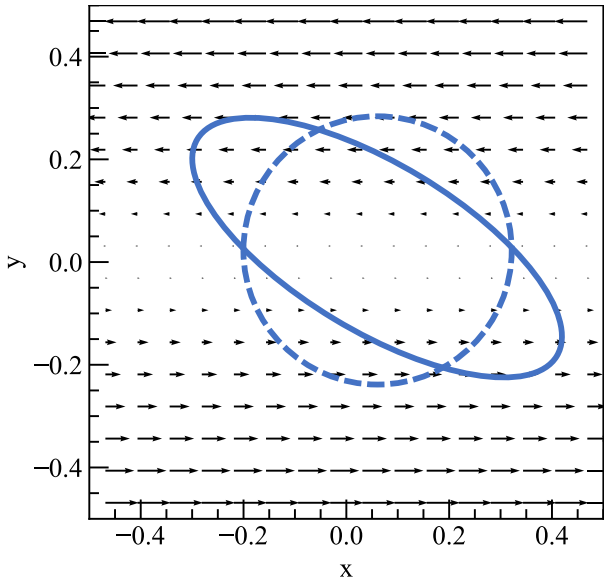

(d) Shear

Figure 3: Illustration of a typical deformation velocity field for interfacial advection.

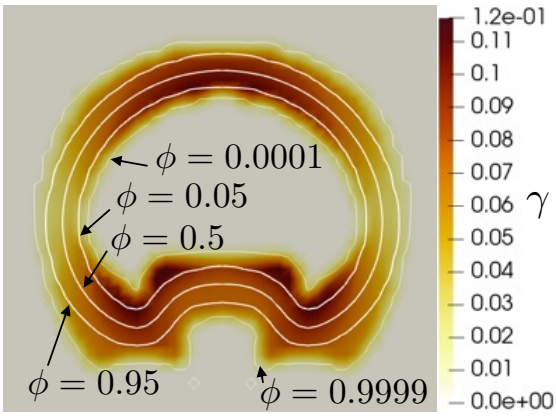

(a) γ

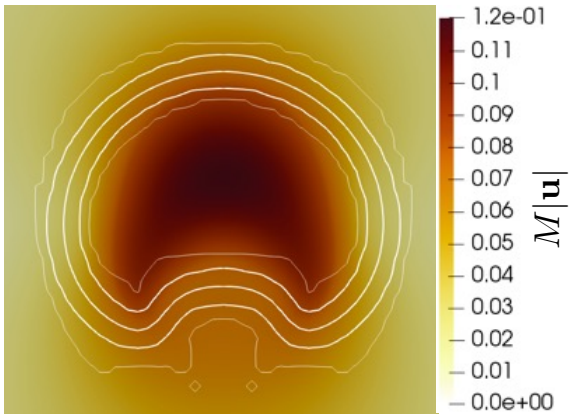

(b) Velocity term

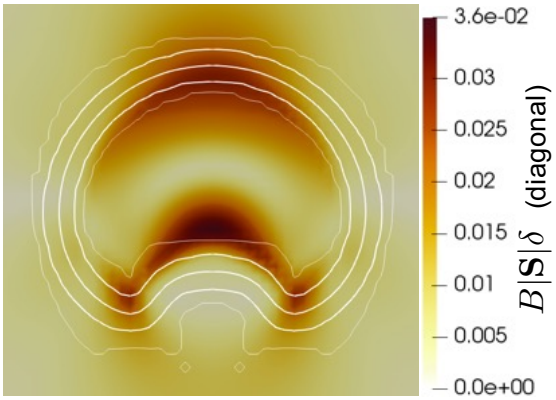

(c) Velocity gradient term (compression and expansion)

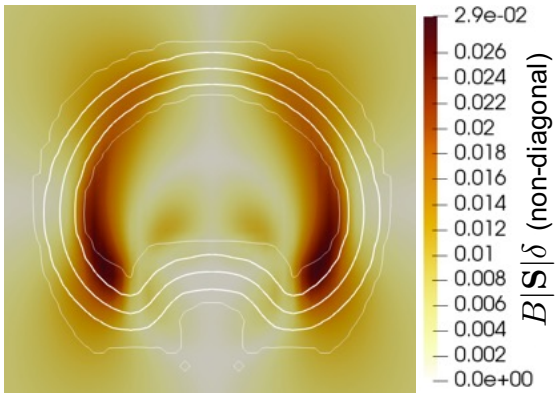

(d) Velocity gradient term (shear)

Figure 4: An example of the spatial distribution of (a) γ, (b) velocity term, (c) compression/expansion component of velocity gradient term, and (d) shear component of velocity gradient term in a single bubble rise calculation. The cross section of case (D) in Fig. 17 are shown for $M = 0.8$, $B = 1.0$, and $\alpha = 0.0001$.

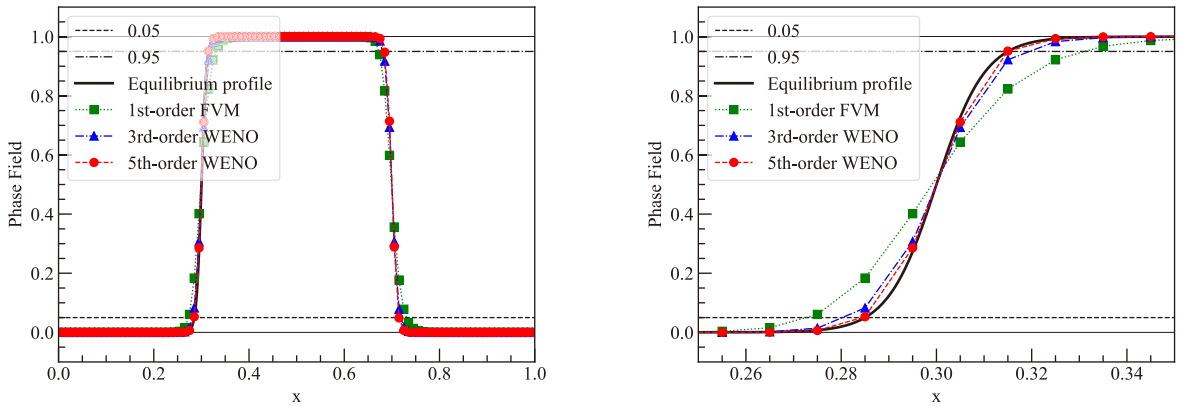

(a) Whole area (b) Zoomed area near the interface

Figure 5: VOF functions are shown for 1D advection tests with $\Delta x = 0.01$, $\Delta t = 0.001$, $u_0 = 1$, and $\gamma = 1$. In (a), a black curve shows the initial profile given by an equilibrium solution with $\delta = 3\Delta x$ and $\lambda = 0.05$. Green, blue, and red curves show profiles after one advection period computed using the first-order FVM scheme, the third-order WENO scheme, and the fifth-order WENO scheme, respectively. (b) shows the same plot near the left interface.

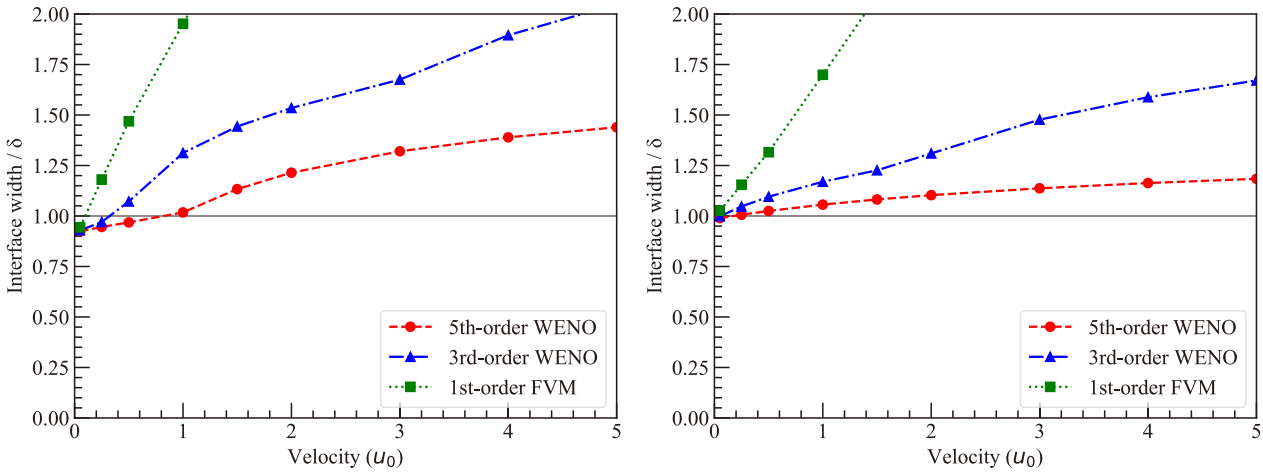

(a) $\delta = 3\Delta x$ (b) $\delta = 4\Delta x$

Figure 6: u_0 scans of the interface width are conducted with $\gamma = 1$. (a) and (b) are computed using the initial equilibrium profiles with $\delta = 3\Delta x$ and $\lambda = 0.05$ and with $\delta = 4\Delta x$ and $\lambda = 0.05$, respectively.

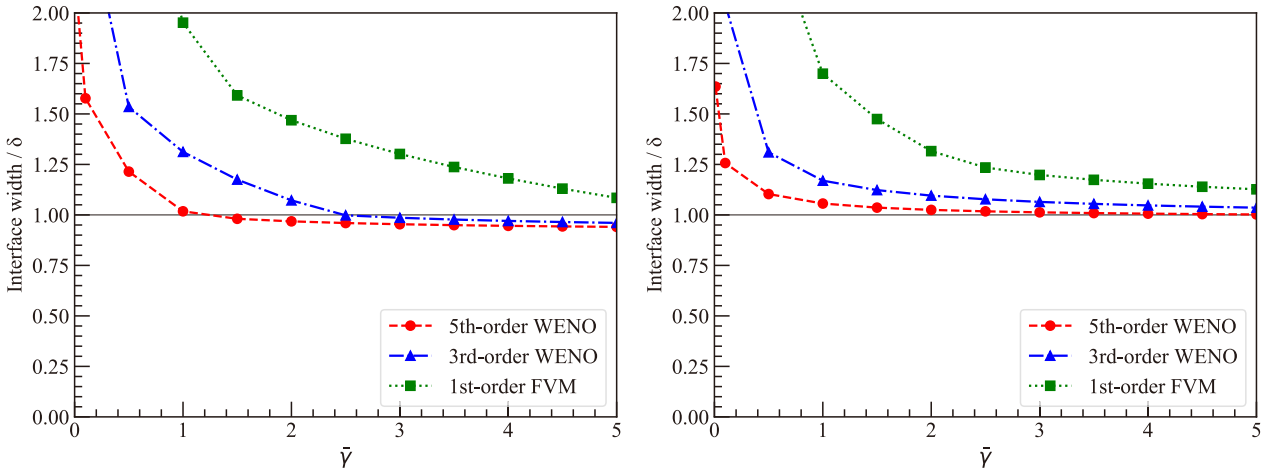

(a) $\delta = 3\Delta x$ (b) $\delta = 4\Delta x$

Figure 7: γ scans of the interface width are conducted with $u_0 = 1$. (a) and (b) are computed using the initial equilibrium profiles with $\delta = 3\Delta x$ and $\lambda = 0.05$ and with $\delta = 4\Delta x$ and $\lambda = 0.05$, respectively.

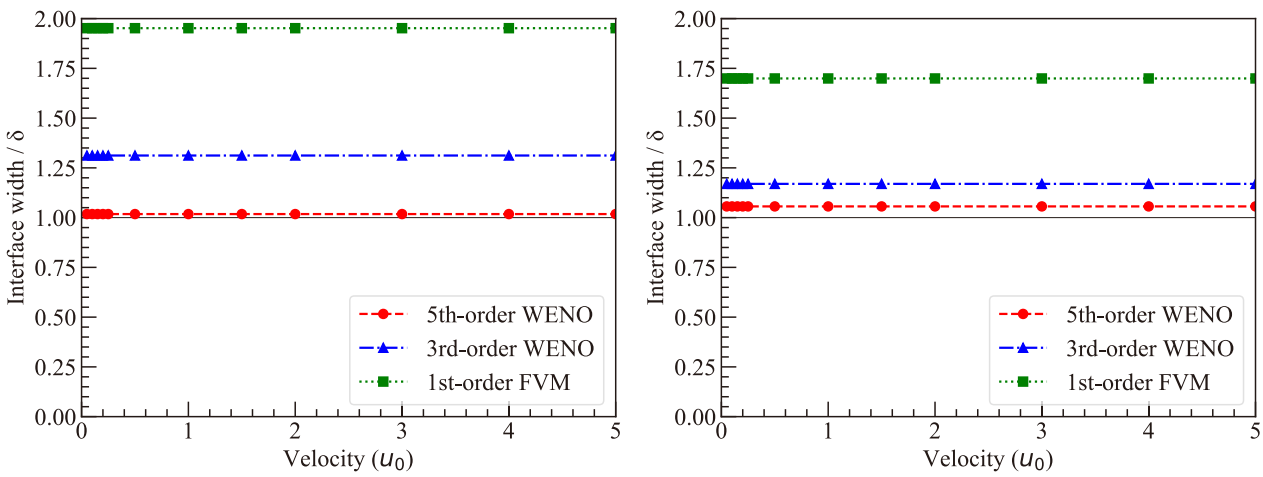

(a) $\delta = 3\Delta x$ (b) $\delta = 4\Delta x$

Figure 8: u_0 scans of the interface width are conducted with $\gamma = u_0$. (a) and (b) are computed using the initial equilibrium profiles with $\delta = 3\Delta x$ and $\lambda = 0.05$ and with $\delta = 4\Delta x$ and $\lambda = 0.05$, respectively.

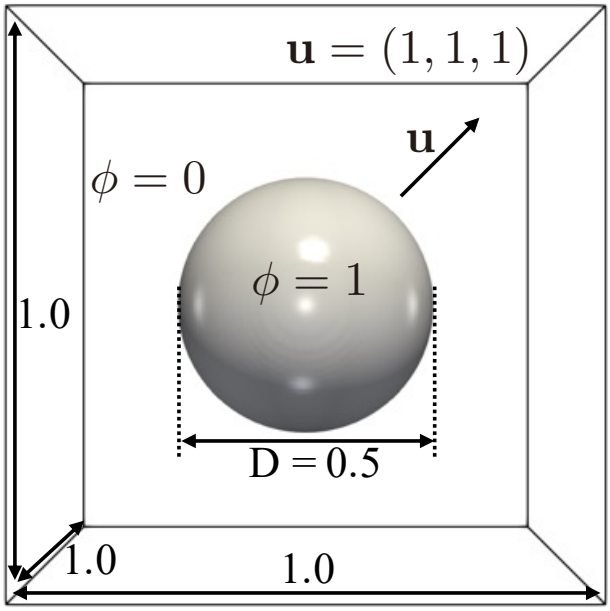

Figure 9: The computational domain and the initial condition of 3D advection tests.

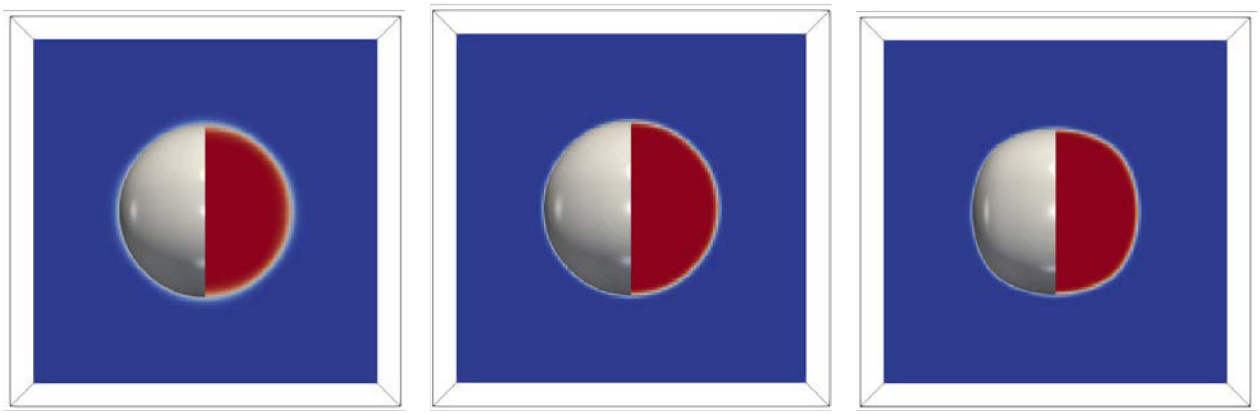

(a) $\gamma = 0.01|\mathbf{u}_{\max}|$ (b) $\gamma = 0.8|\mathbf{u}_{\max}|$ (c) $\gamma = 2.0|\mathbf{u}_{\max}|$

Figure 10: Dependence of the shape and the width of the interface on the phase field parameter γ.

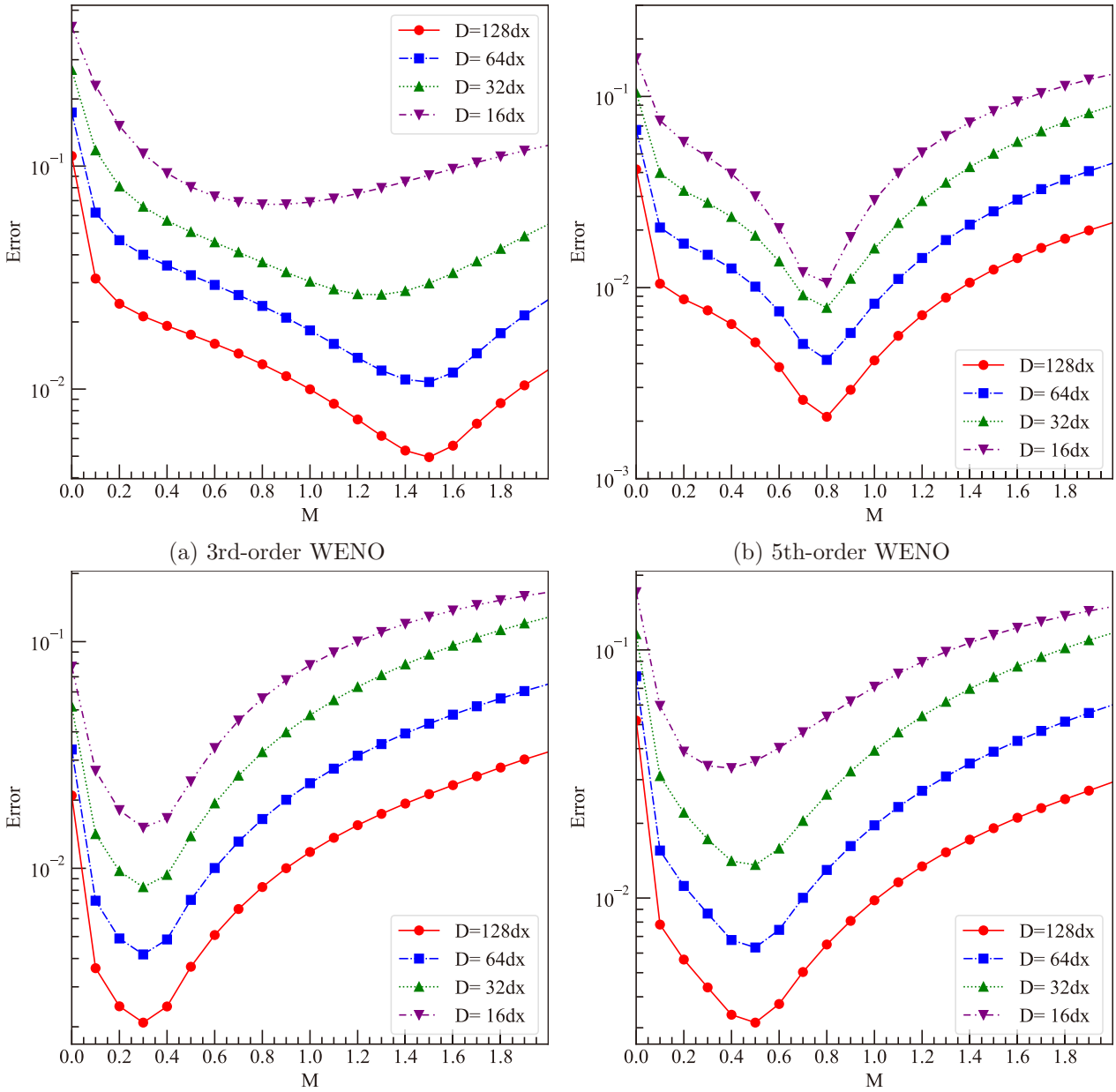

(a) 3rd-order WENO

(b) 5th-order WENO

(c) 7th-order WENO

(d) 3rd-order MUSCL

Figure 11: Dependence of the errors on the phase field parameter $\gamma = M|\mathbf{u}|$ in 3D advection tests with $\delta = 3\Delta x$.

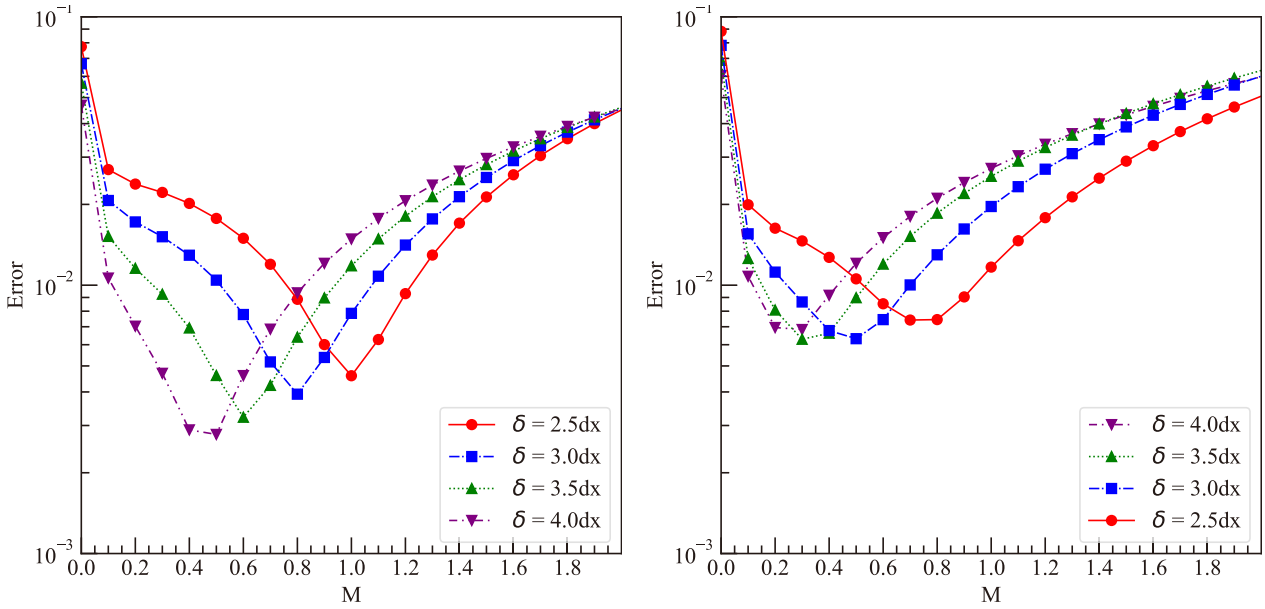

(a) 5th-order WENO ($D = 64\Delta x$)

(b) 3rd-order MUSCL ($D = 64\Delta x$)

Figure 12: Dependence of the error on the interface width δ in 3D advection tests.

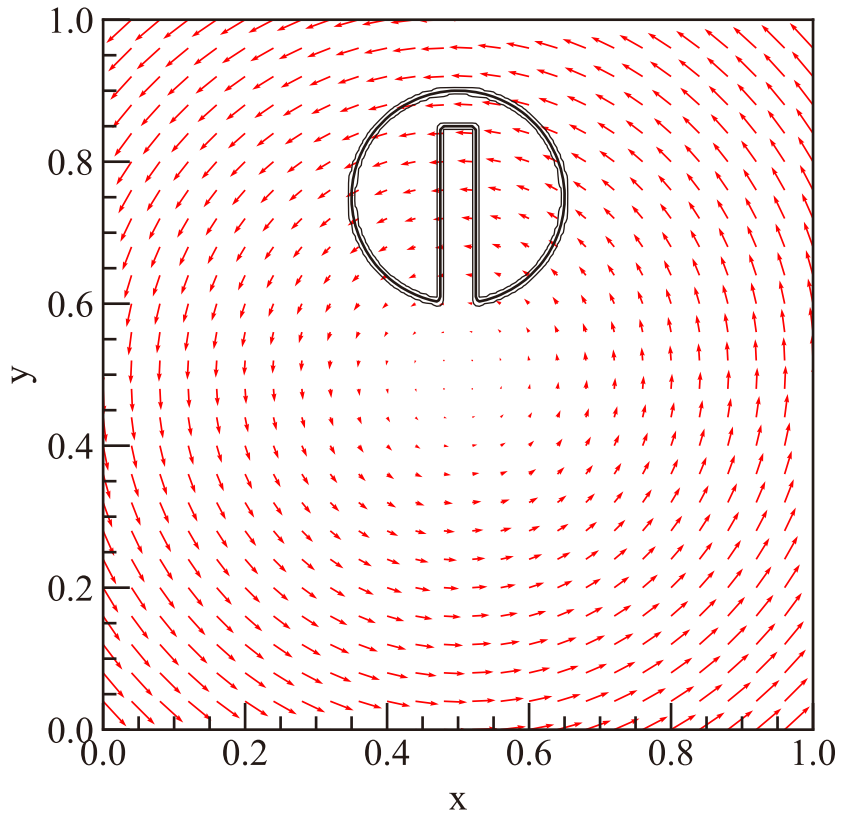

Figure 13: The initial distribution and the rotating velocity field for the Zalesak's test.

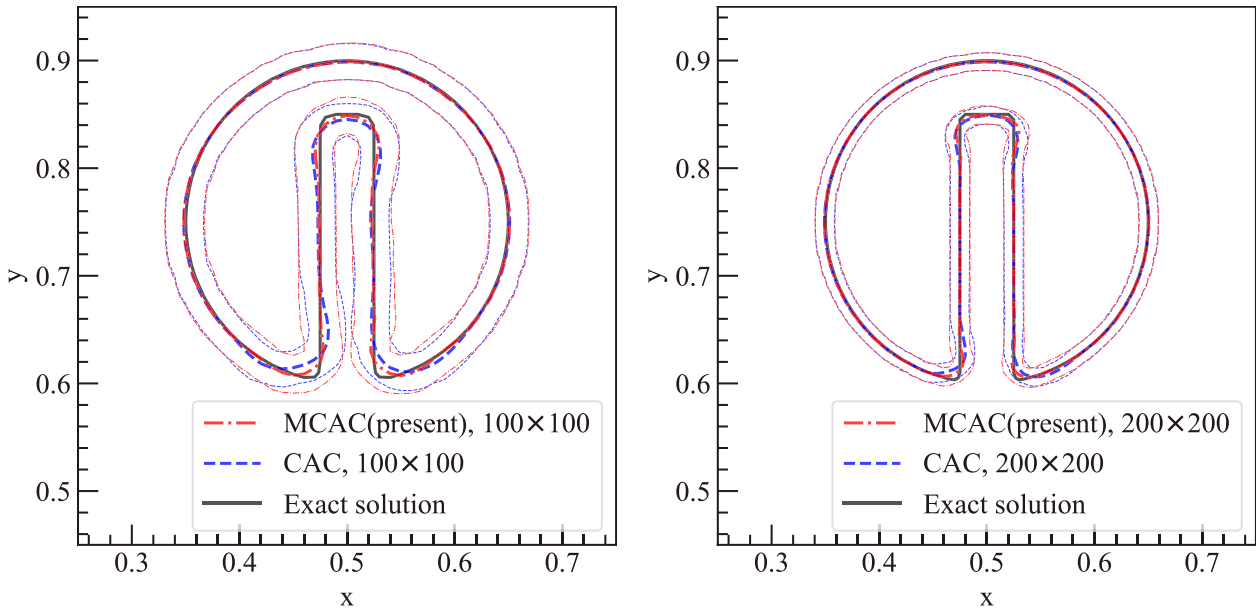

(a) 100 × 100 meshes

(b) 200 × 200 meshes

Figure 14: Contour plots of the VOF function after one rotation period. Contours at $\phi = 0.05, 0.5, 0.95$ are shown.

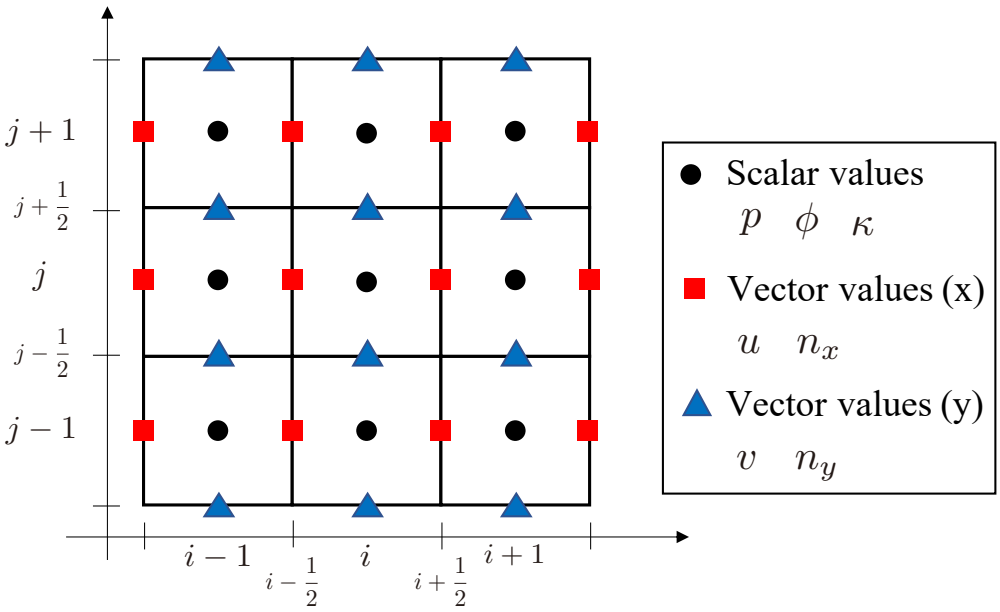

Figure 15: Staggered variable arrangement and index definition.

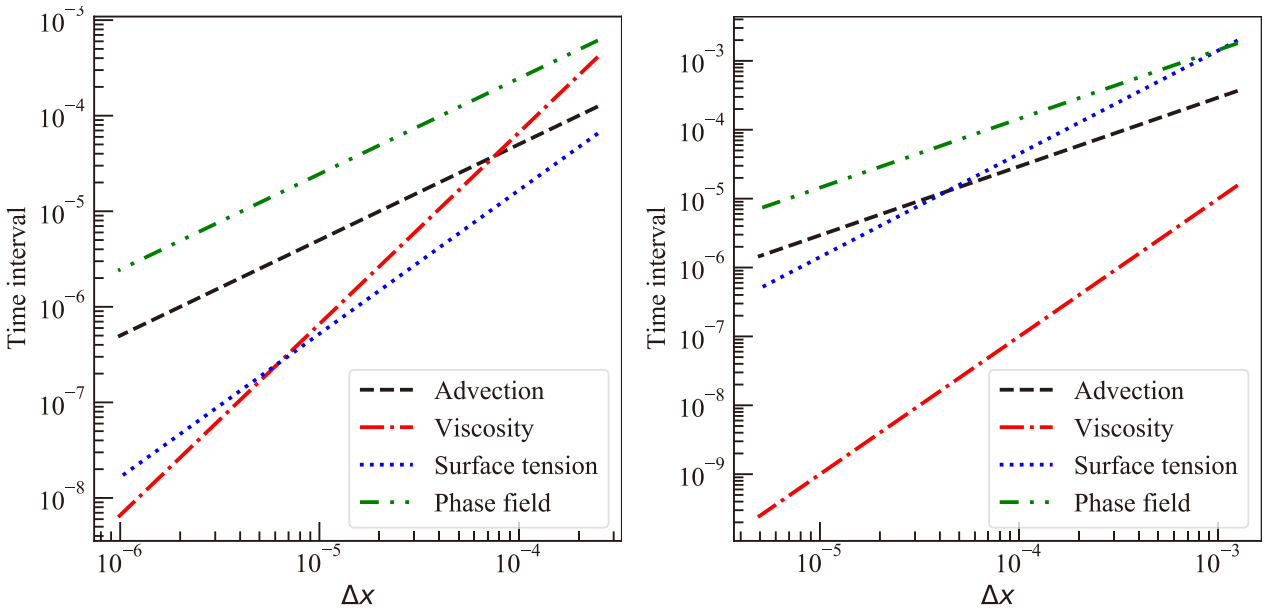

(a) Droplet oscillation (b) Bubble rising (skirted)

Figure 16: Limitations of time step widths in droplet oscillation and bubble rising problems.

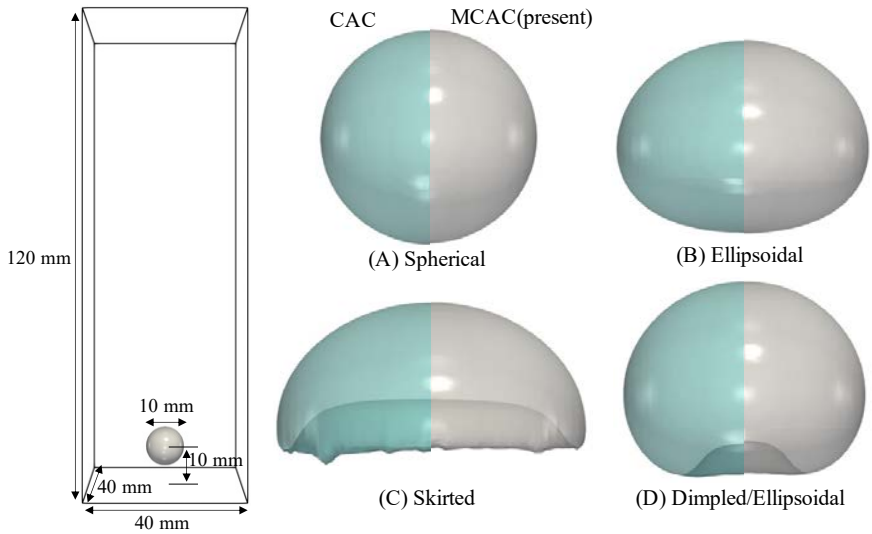

Figure 17: Left shows the computational domain of the bubble rising problem. Right shows comparisons of bubble shapes between the CAC (left half) and MCAC (right half) results. The bubble shapes in four parameter regimes are characterized as (A) Spherical, (B) Ellipsoidal, (C) Skirted, and (D) Dimpled. The isosurface is shown for $\phi = 0.5$.

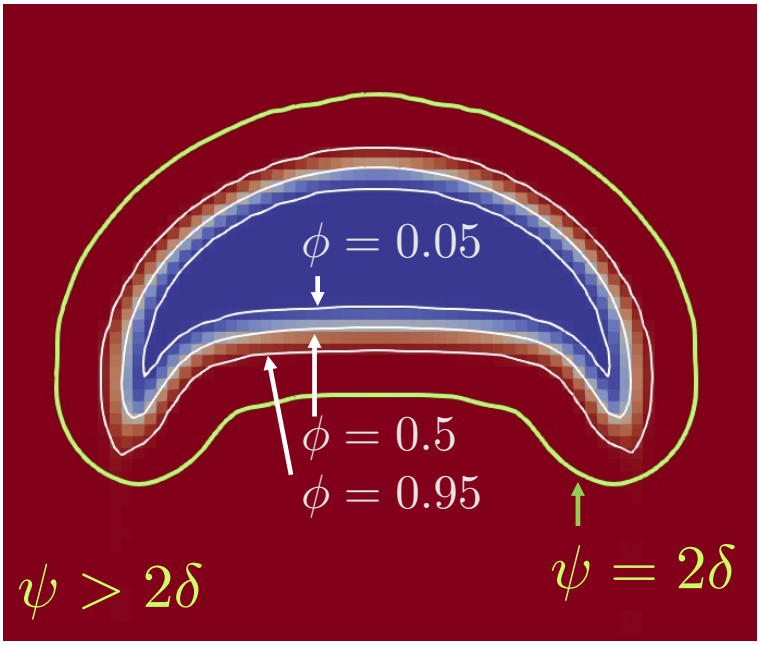

Figure 18: Evaluation area of bubble volume error (Case-C, Skirted, MCAC, $D_b/\Delta x = 32$, $B = 1$). The four contour lines are $\phi = 0.05, 0.5, 0.95$, and $\psi = 2\delta$, respectively.

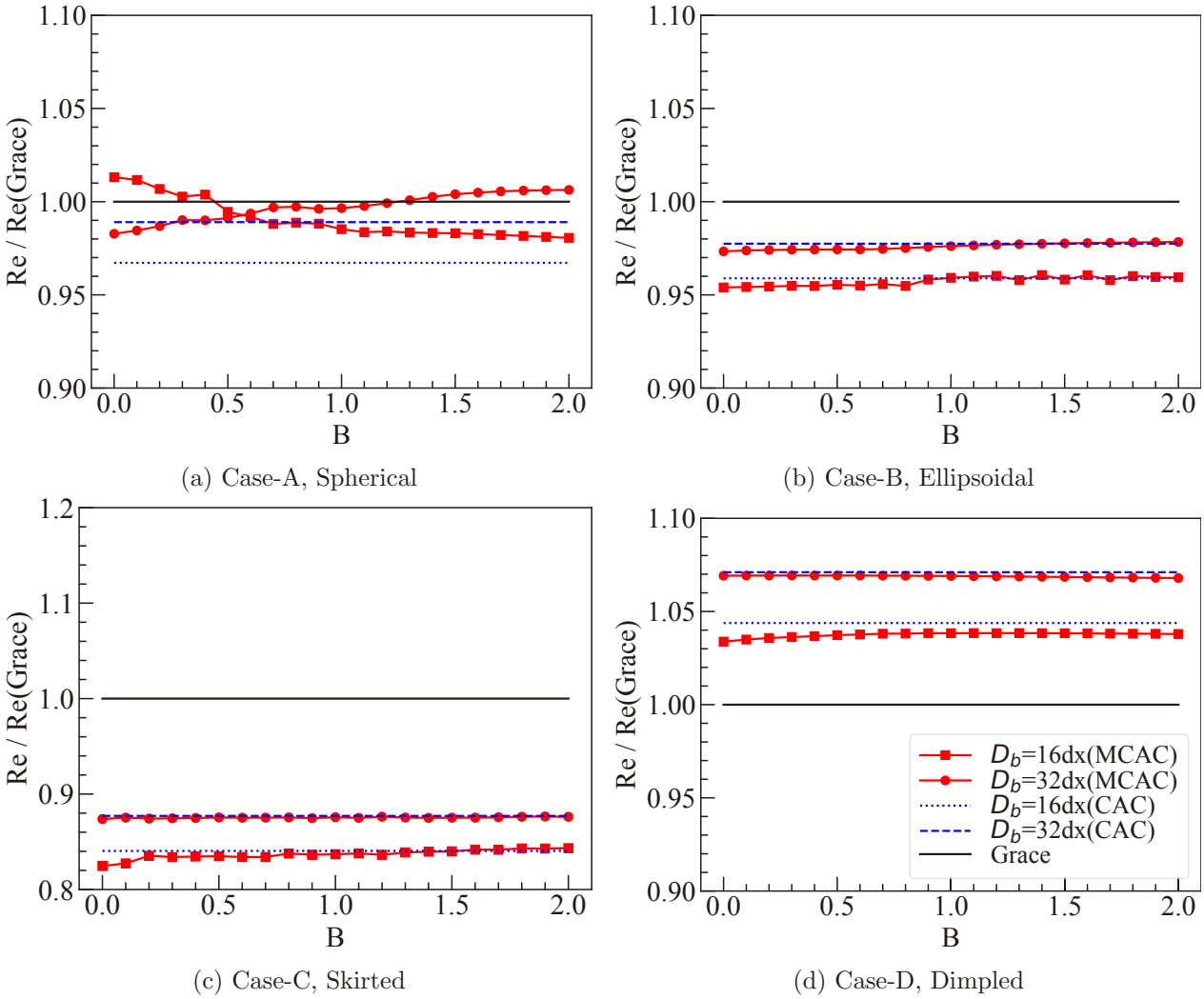

(a) Case-A, Spherical

(b) Case-B, Ellipsoidal

(c) Case-C, Skirted

(d) Case-D, Dimpled

Figure 19: Test results using the MCAC method. The bubble Reynolds number is plotted against the parameter of velocity gradient term B. Also shown are the results using the CAC method. The bubble Reynolds number Re is normalized by the experimental value Re (Grace).

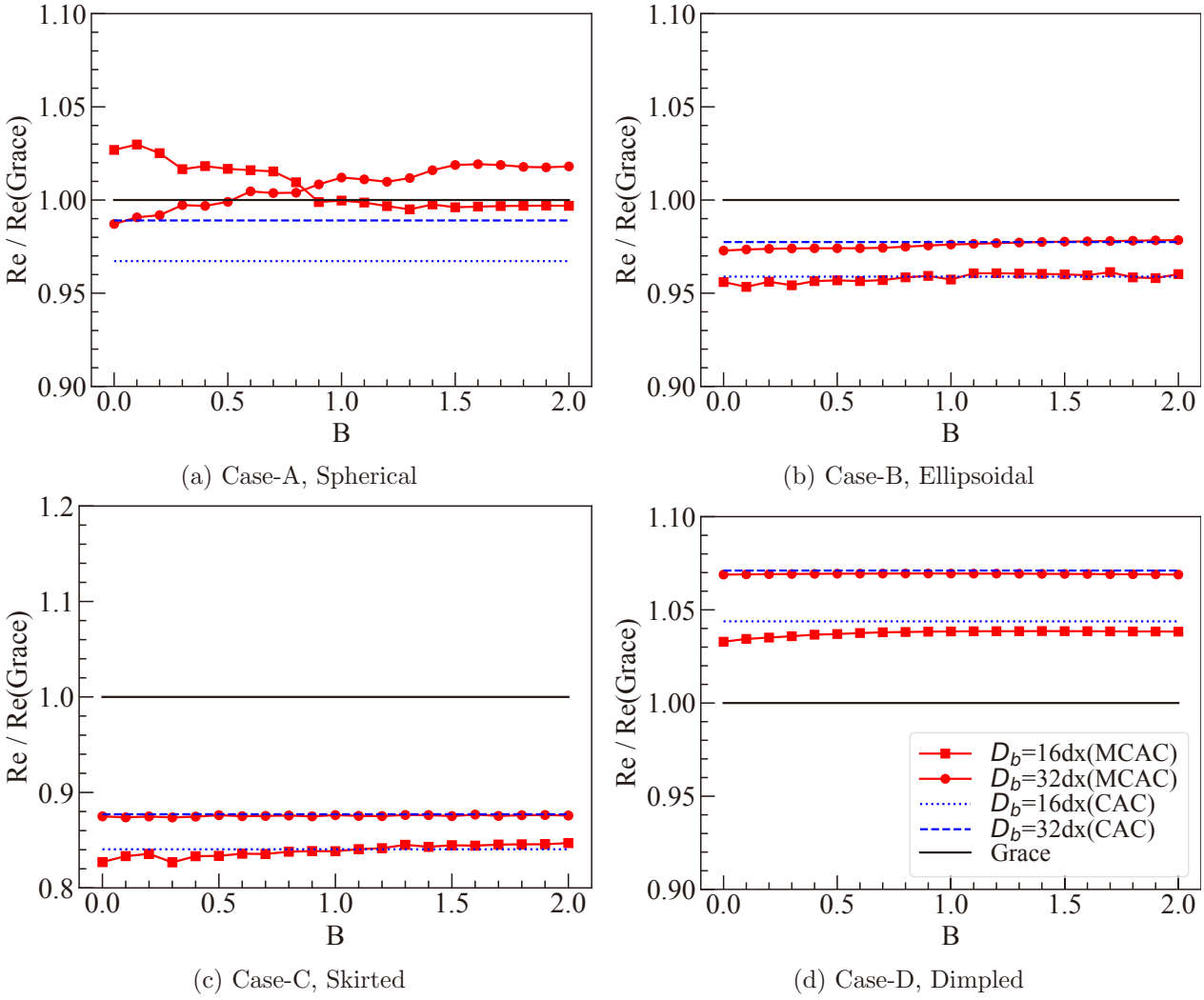

(a) Case-A, Spherical

(b) Case-B, Ellipsoidal

(c) Case-C, Skirted

(d) Case-D, Dimpled

Figure 20: Test results using the MCAC-CO method. The same definition as Fig.19 is used.

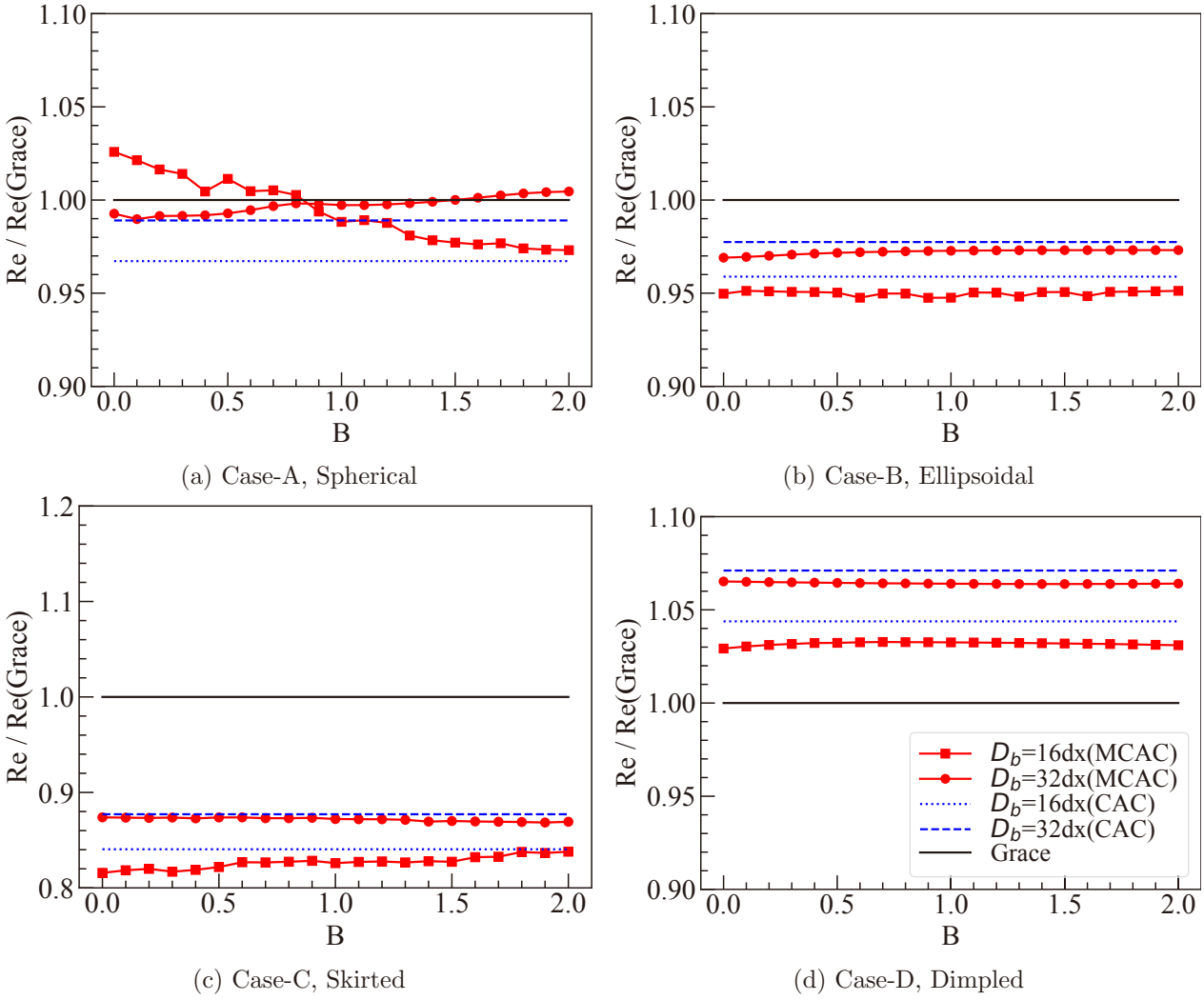

(a) Case-A, Spherical

(b) Case-B, Ellipsoidal

(c) Case-C, Skirted

(d) Case-D, Dimpled

Figure 21: Test results using the MCAC-MR method. The same definition as Fig.19 is used.

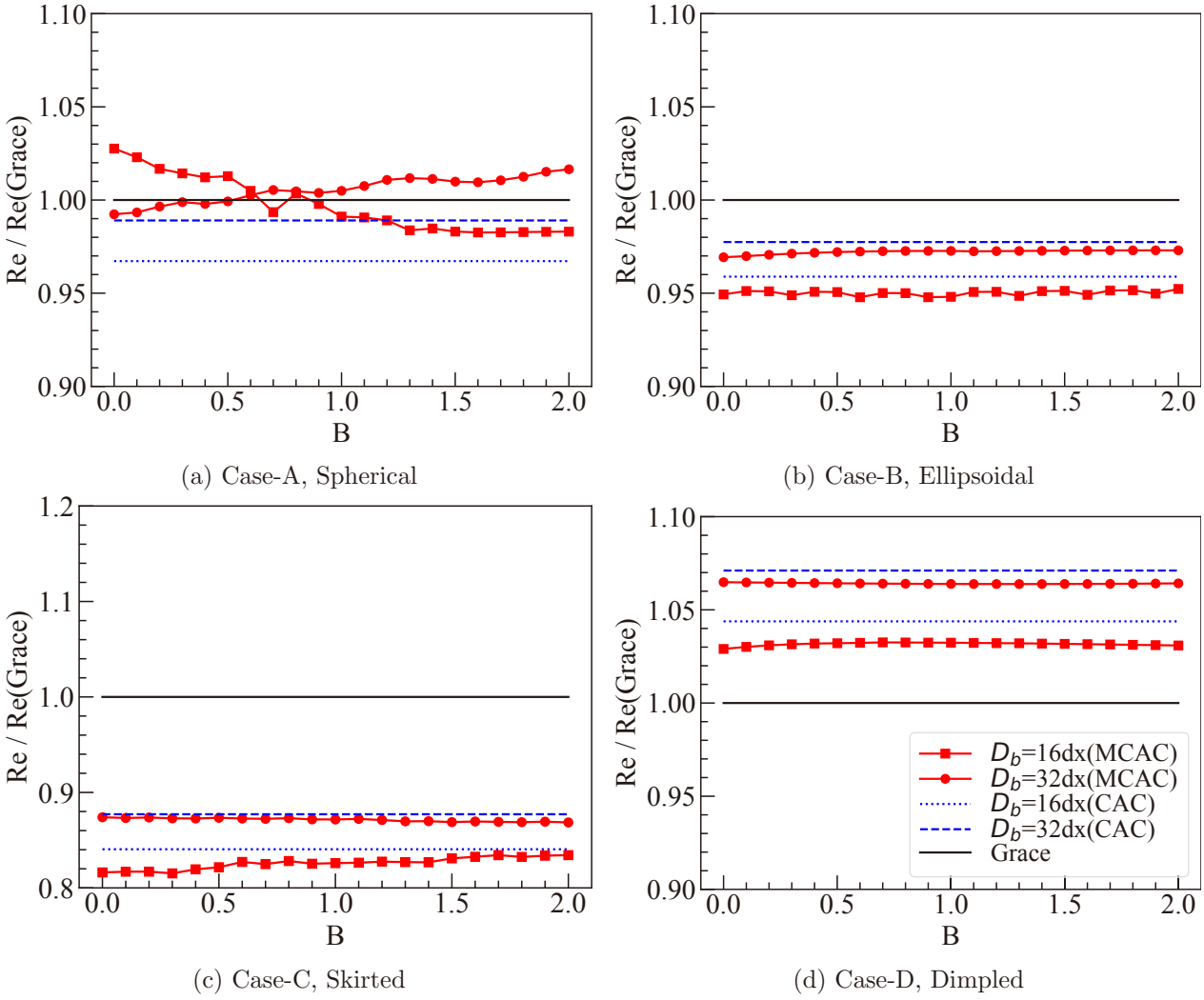

(a) Case-A, Spherical

(b) Case-B, Ellipsoidal

(c) Case-C, Skirted

(d) Case-D, Dimpled

Figure 22: Test results using the MCAC-COMR method. The same definition as Fig.19 is used.

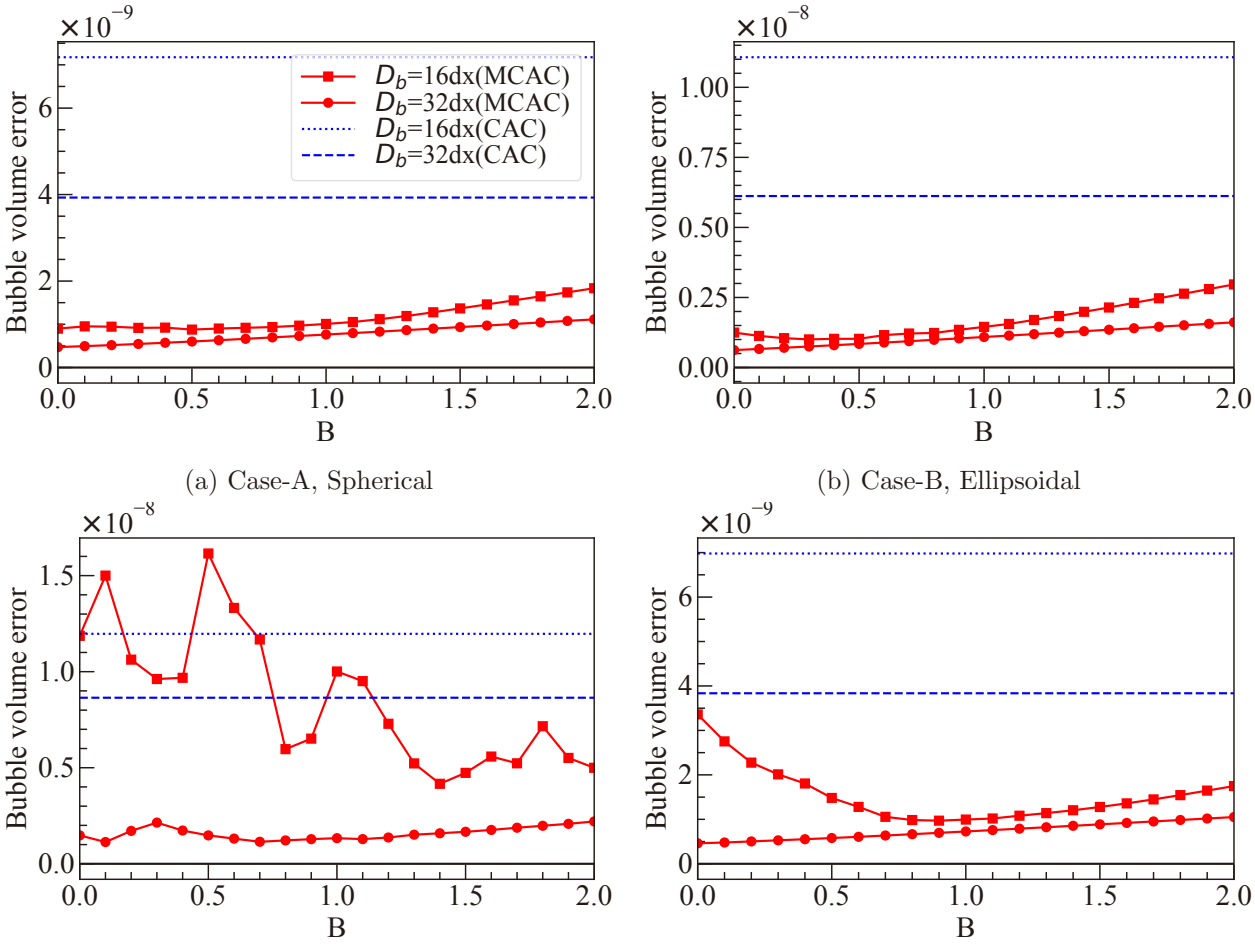

(a) Case-A, Spherical

(b) Case-B, Ellipsoidal

(c) Case-C, Skirted

(d) Case-D, Dimpled

Figure 23: Test results using the MCAC method. The bubble volume error $\int_\Omega |1-\phi| dV$ is plotted against the parameter of velocity gradient term B. Also shown are the results using the CAC method.

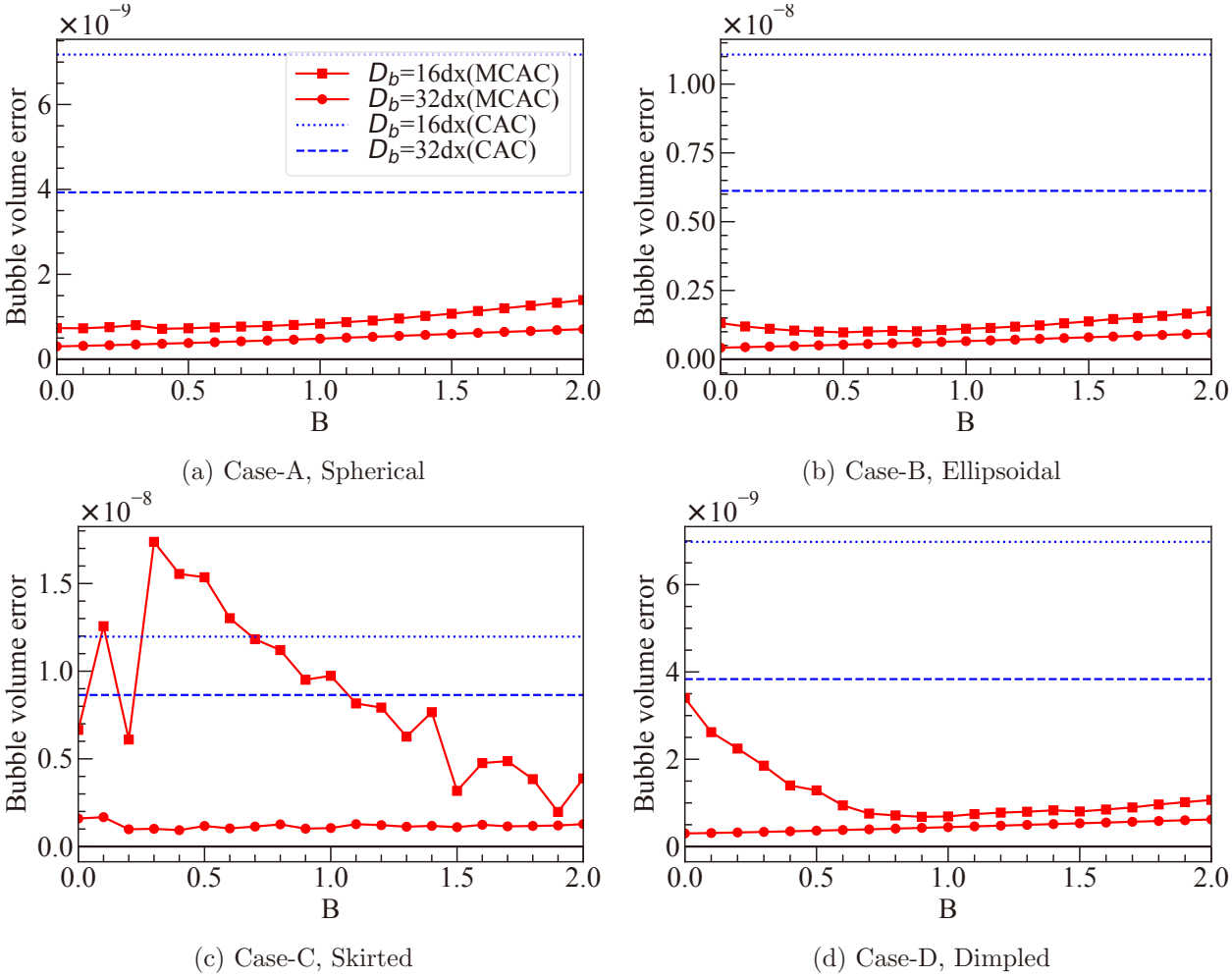

(a) Case-A, Spherical

(b) Case-B, Ellipsoidal

(c) Case-C, Skirted

(d) Case-D, Dimpled

Figure 24: Test results using the MCAC-CO method. The same definition as Fig.23 is used.

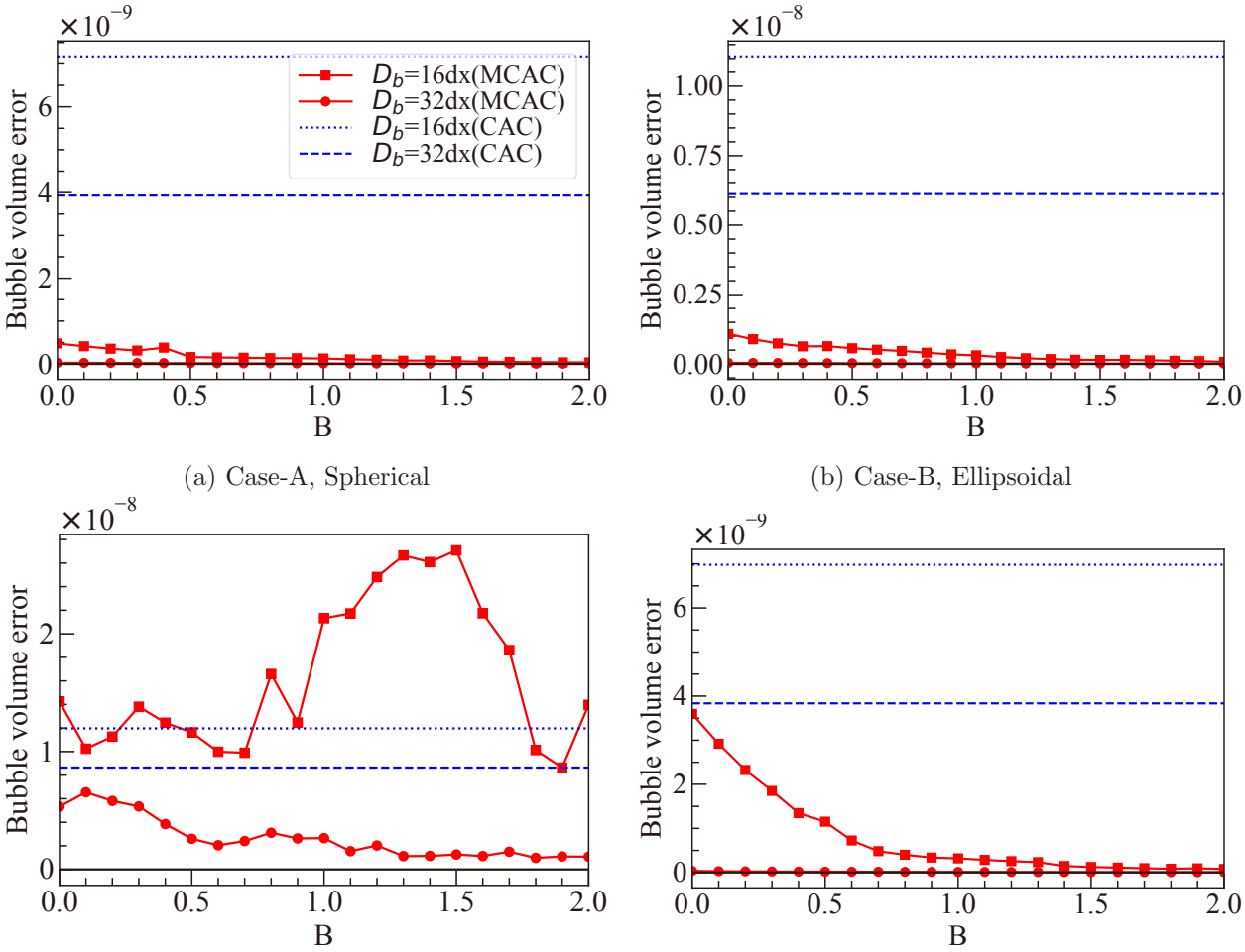

(a) Case-A, Spherical

(b) Case-B, Ellipsoidal

(c) Case-C, Skirted

(d) Case-D, Dimpled

Figure 25: Test results using the MCAC-MR method. The same definition as Fig.23 is used.

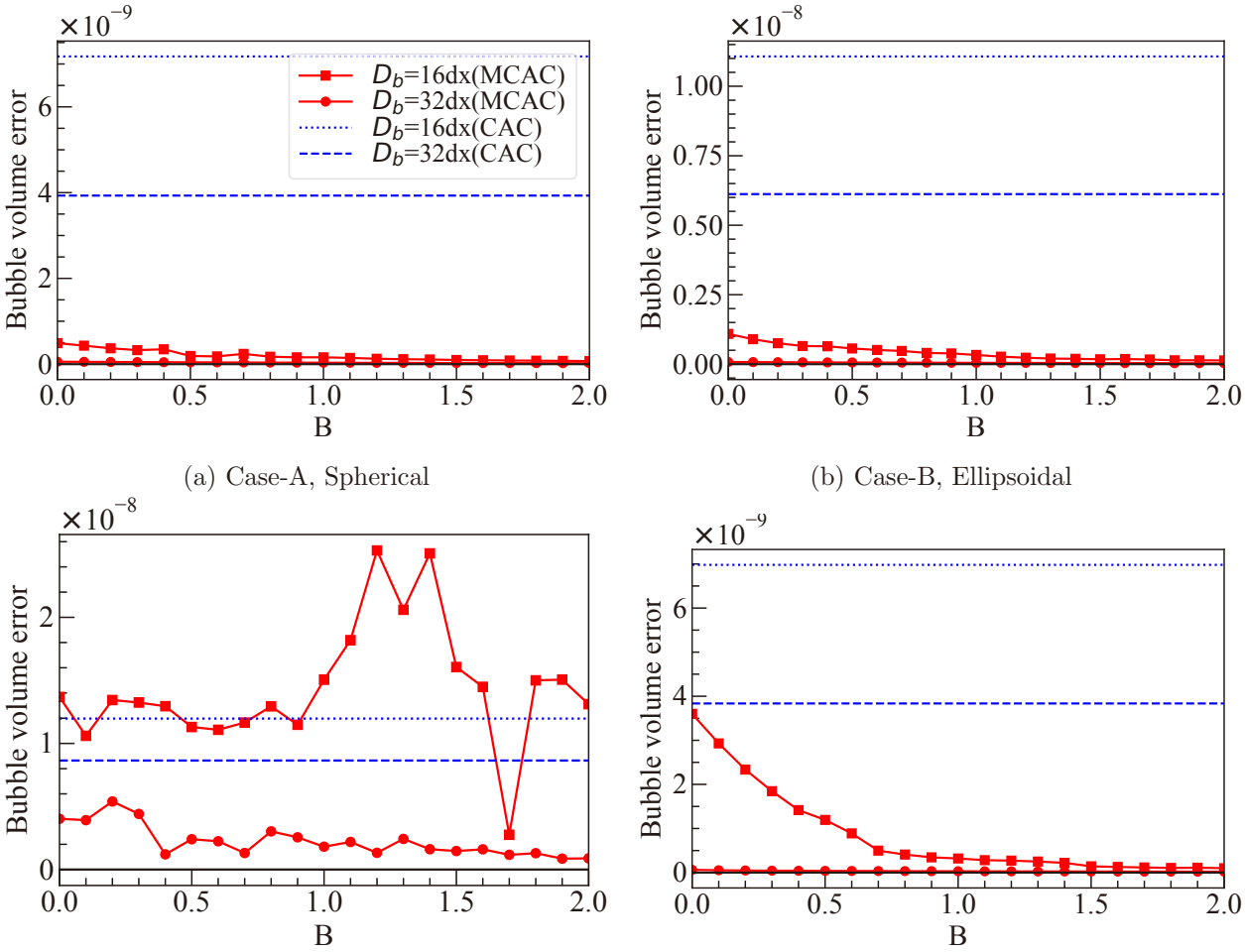

(a) Case-A, Spherical

(b) Case-B, Ellipsoidal

(c) Case-C, Skirted

(d) Case-D, Dimpled

Figure 26: Test results using the MCAC-COMR method. The same definition as Fig.23 is used.

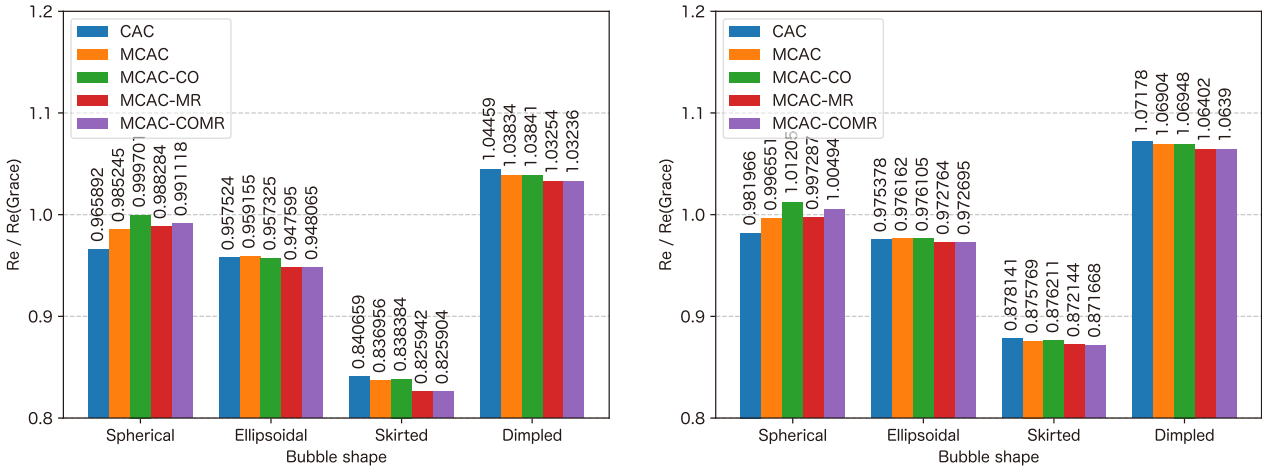

(a) D_b=16dx (b) D_b=32dx

Figure 27: Comparisons of the bubble Reynolds numbers obtained using the CAC, MCAC, MCAC-CO, MCAC-MR, and MCAC-COMR methods with $M = 0.8$, $B = 1.0$, and the grid resolution of $D_b/\Delta x = 16$, 32, where D_b is the diameter of the initial spherical bubble.

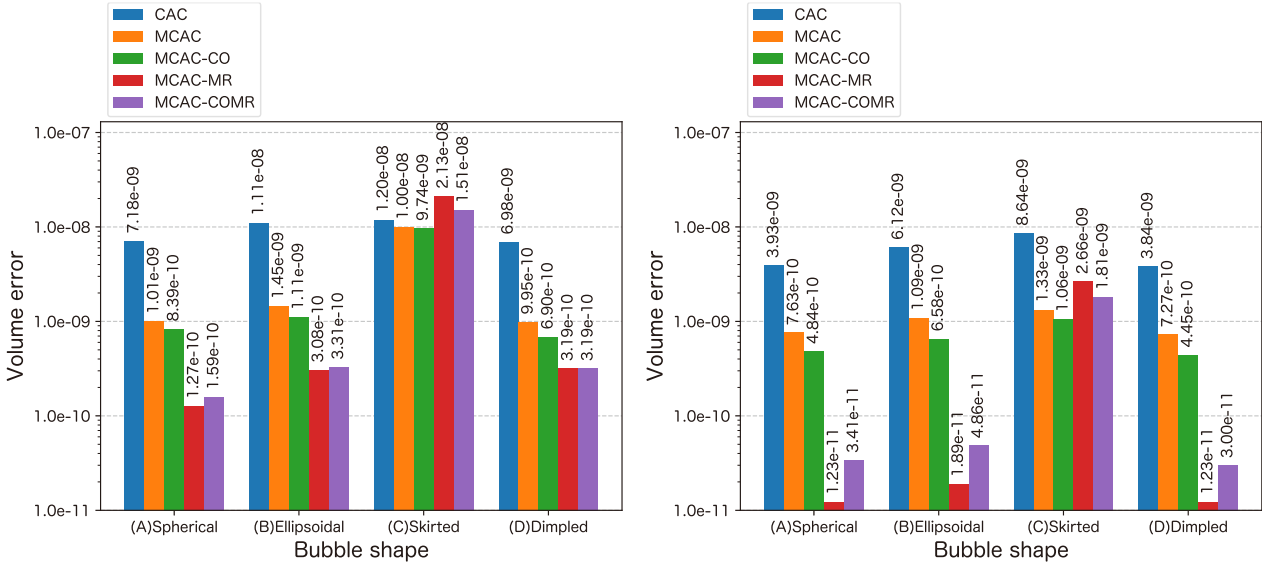

(a) D_b=16dx (b) D_b=32dx

Figure 28: Comparisons of the bubble volume error for the CAC, MCAC, MCAC-CO, MCAC-MR, and MCAC-COMR methods with $M = 0.8$, $B = 1.0$, and the grid resolution of $D_b/\Delta x = 16$, 32.

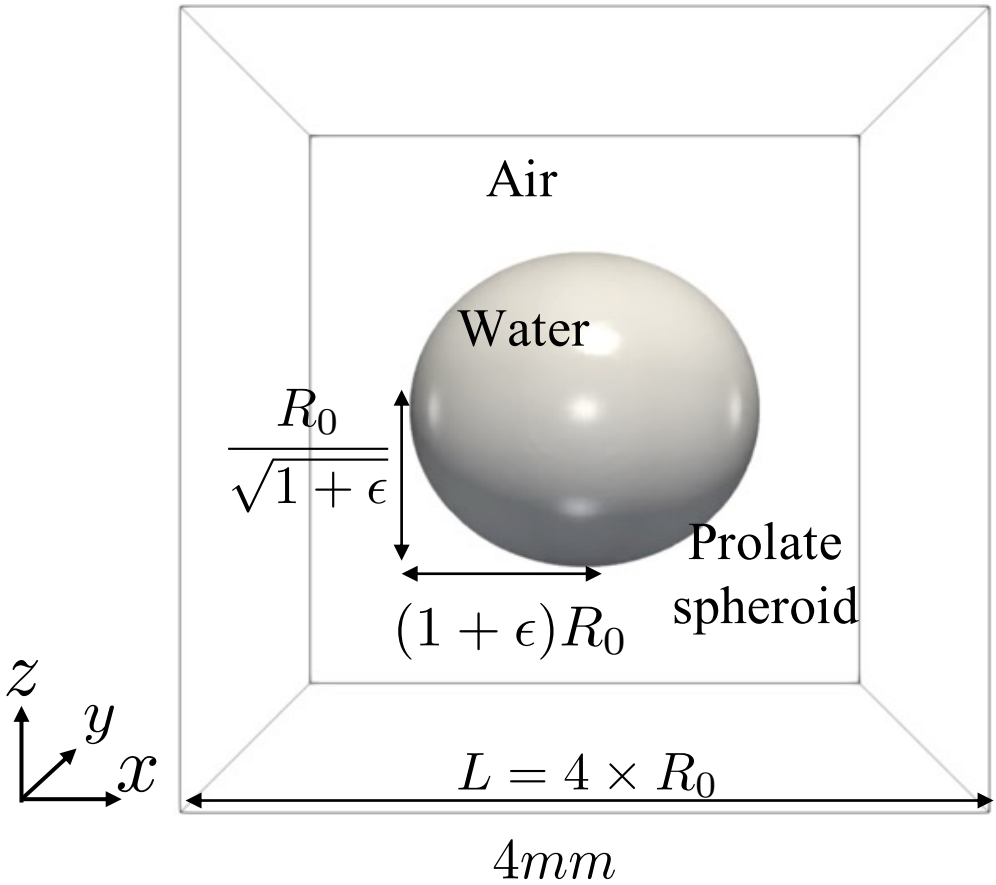

Figure 29: Set up for 3D water droplet oscillation simulation.

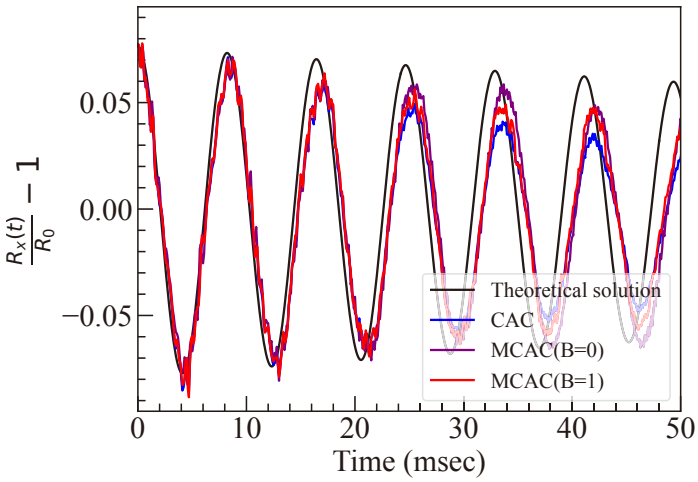

(a) $D = 32\Delta x$

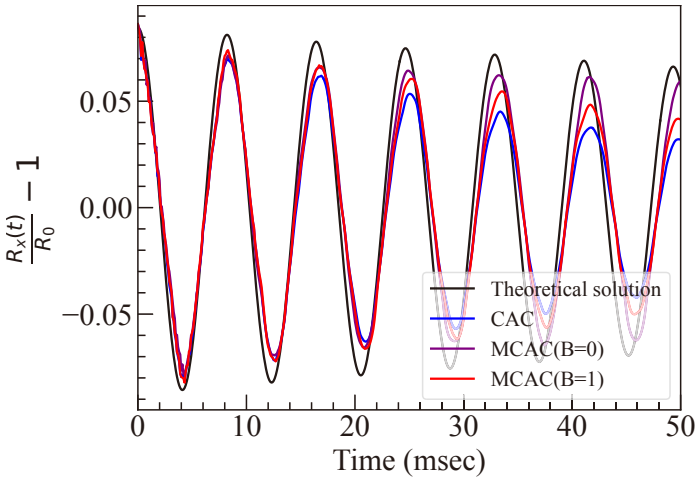

(b) $D = 64\Delta x$

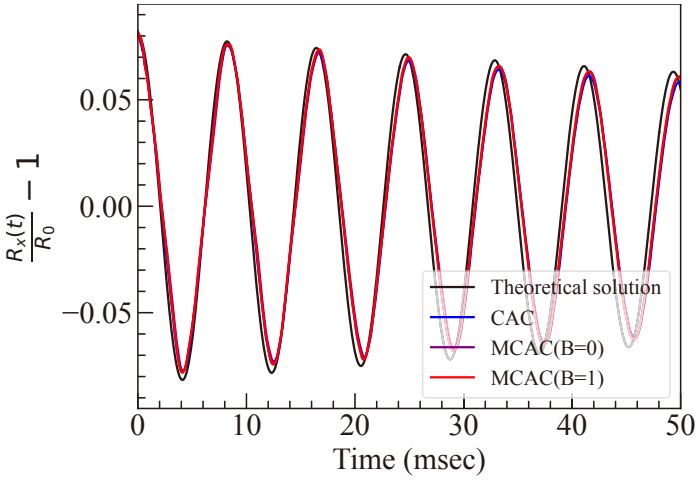

(c) $D = 128\Delta x$

Figure 30: The time histories of the droplet radius in droplet oscillation tests.

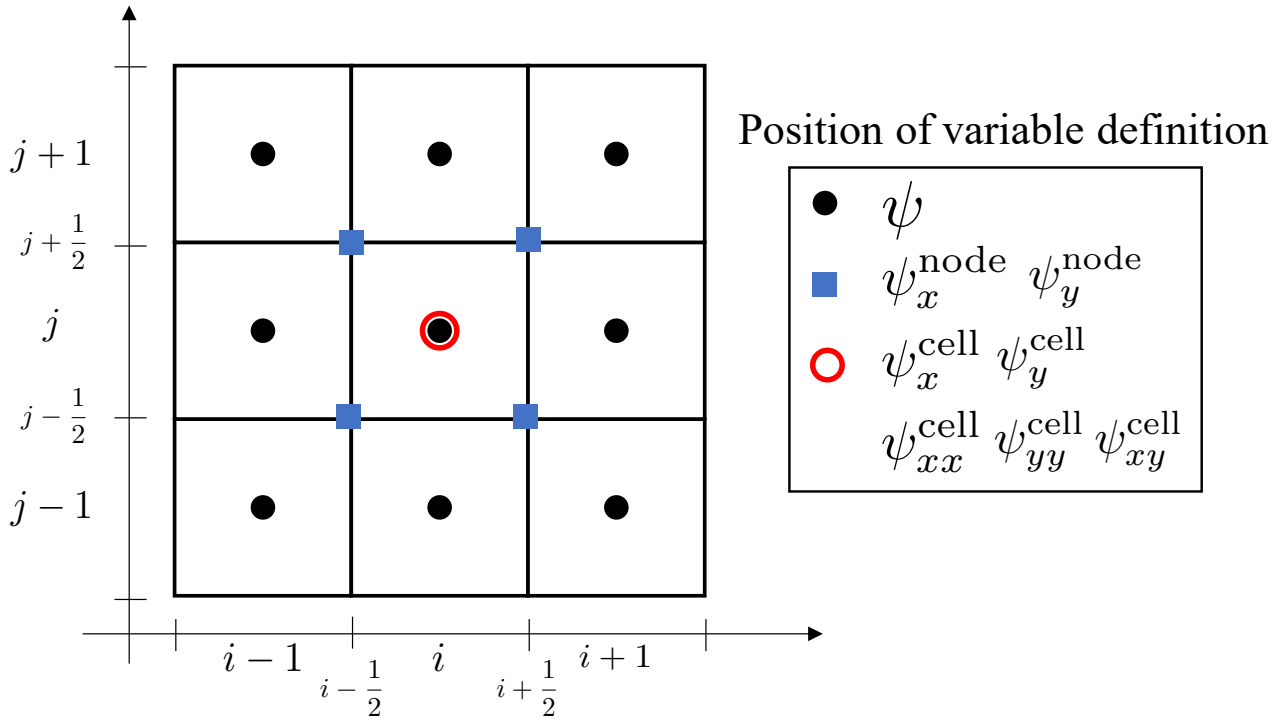

Figure 31: Arrangement of spatial gradient variables of volume fraction for curvature calculations.

Appendix

In computing the surface tension force, an evaluation of the curvature has a significant influence on the accuracy of the interface geometry. The curvature of the gas-liquid two-phase interface is defined by the divergence of the unit normal vector as in the following equation,

$$\kappa = -\nabla \cdot \mathbf{n}. \tag{39}$$

The unit normal vector is computed as $\mathbf{n} = \nabla\phi/|\nabla\phi|$ using the VOF function, which is smoothed in the same manner as the computation of the normal vector in the phase field equation, and redefined as $\mathbf{n}' = \nabla\psi/|\nabla\psi|$ using the SDF in Eq.6, and the curvature is calculated as

$$\kappa = -\nabla \cdot \left(\frac{\nabla\psi}{|\nabla\psi|} \right). \tag{40}$$

As the curvature is non-conservative, it does not need to be discretized in a conservative form. Eq.(40) can be expanded as

$$\kappa = -\frac{1}{|\nabla\psi|} \left(\nabla^2\psi - \frac{\nabla\psi \cdot \nabla|\nabla\psi|}{|\nabla\psi|} \right). \tag{41}$$

Eq. (41) is then discretized as

$$\begin{aligned} \kappa = -\big[&\psi_x^2(\psi_{yy} + \psi_{zz}) + \psi_y^2(\psi_{zz} + \psi_{xx}) + \psi_z^2(\psi_{xx} + \psi_{yy}) \\ &-2(\psi_x\psi_y\psi_{xy} + \psi_y\psi_z\psi_{yz} + \psi_z\psi_x\psi_{zx})\big] / (\psi_x^2 + \psi_y^2 + \psi_z^2)^{\frac{3}{2}}, \end{aligned} \tag{42}$$

where ψ_x is the x derivative of ψ. The curvature κ is defined at the cell-center and is computed using ψ on $3 \times 3 \times 3$ cells in the following three steps. Firstly, the spatial gradient of ψ is computed on the cell-node as follows,

$$\begin{aligned} \psi^{\text{node}}_{x,i-\frac{1}{2},j-\frac{1}{2},k-\frac{1}{2}} = \frac{1}{4\Delta x}(&\psi_{i,j,k} - \psi_{i-1,j,k} + \psi_{i,j-1,k} - \psi_{i-1,j-1,k} \\ &+\psi_{i,j,k-1} - \psi_{i-1,j,k-1} + \psi_{i,j-1,k-1} - \psi_{i-1,j-1,k-1}), \end{aligned} \tag{43}$$

$$\begin{aligned} \psi^{\text{node}}_{y,i-\frac{1}{2},j-\frac{1}{2},k-\frac{1}{2}} = \frac{1}{4\Delta y}(&\psi_{i,j,k} - \psi_{i,j-1,k} + \psi_{i-1,j,k} - \psi_{i-1,j-1,k} \\ &+\psi_{i,j,k-1} - \psi_{i,j-1,k-1} + \psi_{i-1,j,k-1} - \psi_{i-1,j-1,k-1}), \end{aligned} \tag{44}$$

$$\begin{aligned} \psi^{\text{node}}_{z,i-\frac{1}{2},j-\frac{1}{2},k-\frac{1}{2}} = \frac{1}{4\Delta z}(&\psi_{i,j,k} - \psi_{i,j,k-1} + \psi_{i-1,j,k} - \psi_{i-1,j,k-1} \\ &+\psi_{i,j-1,k} - \psi_{i,j-1,k-1} + \psi_{i-1,j-1,k} - \psi_{i-1,j-1,k-1}). \end{aligned} \tag{45}$$

Next, the first-order derivative of ψ defined at the cell-node is used to calculate the derivative at the cell center,

$$\begin{aligned} \psi^{\text{cell}}_{x,i,j,k} = \frac{1}{8}(&\psi^{\text{node}}_{x,i+\frac{1}{2},j+\frac{1}{2},k+\frac{1}{2}} + \psi^{\text{node}}_{x,i+\frac{1}{2},j-\frac{1}{2},k+\frac{1}{2}} + \psi^{\text{node}}_{x,i+\frac{1}{2},j+\frac{1}{2},k-\frac{1}{2}} \\ &+\psi^{\text{node}}_{x,i+\frac{1}{2},j-\frac{1}{2},k-\frac{1}{2}} + \psi^{\text{node}}_{x,i-\frac{1}{2},j+\frac{1}{2},k+\frac{1}{2}} + \psi^{\text{node}}_{x,i-\frac{1}{2},j-\frac{1}{2},k+\frac{1}{2}} \\ &+\psi^{\text{node}}_{x,i-\frac{1}{2},j+\frac{1}{2},k-\frac{1}{2}} + \psi^{\text{node}}_{x,i-\frac{1}{2},j-\frac{1}{2},k-\frac{1}{2}}), \end{aligned} \tag{46}$$

$$\begin{aligned}\psi^{\text{cell}}_{xx,i,j,k} = \frac{1}{4\Delta x}(&\psi^{\text{node}}_{x,i+\frac{1}{2},j+\frac{1}{2},k+\frac{1}{2}} - \psi^{\text{node}}_{x,i-\frac{1}{2},j+\frac{1}{2},k+\frac{1}{2}} + \psi^{\text{node}}_{x,i+\frac{1}{2},j-\frac{1}{2},k+\frac{1}{2}} \\ &-\psi^{\text{node}}_{x,i-\frac{1}{2},j-\frac{1}{2},k+\frac{1}{2}} + \psi^{\text{node}}_{x,i+\frac{1}{2},j+\frac{1}{2},k-\frac{1}{2}} - \psi^{\text{node}}_{x,i-\frac{1}{2},j+\frac{1}{2},k-\frac{1}{2}} \\ &+\psi^{\text{node}}_{x,i+\frac{1}{2},j-\frac{1}{2},k-\frac{1}{2}} - \psi^{\text{node}}_{x,i-\frac{1}{2},j-\frac{1}{2},k-\frac{1}{2}}),\end{aligned} \tag{47}$$

$$\begin{aligned}\psi^{\text{cell}}_{xy,i,j,k} = \frac{1}{4\Delta y}(&\psi^{\text{node}}_{x,i+\frac{1}{2},j+\frac{1}{2},k+\frac{1}{2}} - \psi^{\text{node}}_{x,i+\frac{1}{2},j-\frac{1}{2},k+\frac{1}{2}} + \psi^{\text{node}}_{x,i+\frac{1}{2},j+\frac{1}{2},k-\frac{1}{2}} \\ &-\psi^{\text{node}}_{x,i+\frac{1}{2},j-\frac{1}{2},k-\frac{1}{2}} + \psi^{\text{node}}_{x,i-\frac{1}{2},j+\frac{1}{2},k+\frac{1}{2}} - \psi^{\text{node}}_{x,i-\frac{1}{2},j-\frac{1}{2},k+\frac{1}{2}} \\ &+\psi^{\text{node}}_{x,i-\frac{1}{2},j+\frac{1}{2},k-\frac{1}{2}} - \psi^{\text{node}}_{x,i-\frac{1}{2},j-\frac{1}{2},k-\frac{1}{2}}).\end{aligned} \tag{48}$$

The same procedure is done for gradients such as $\psi_y, \psi_z, \psi_{yy}, \psi_{zz}$, ψ_{yz}, and ψ_{zx}. Figure 31 shows a 2D example of gradients explained above. Finally, the curvature κ is calculated using the spatial gradient of ψ defined at the cell center

$$\begin{aligned}\kappa_{i,j,k} = -&\left[\psi_x^2(\psi_{yy}+\psi_{zz}) + \psi_y^2(\psi_{zz}+\psi_{xx}) + \psi_z^2(\psi_{xx}+\psi_{yy})\right. \\ &\left.-2(\psi_x\psi_y\psi_{xy} + \psi_y\psi_z\psi_{yz} + \psi_z\psi_x\psi_{zx})\right]/(\psi_x^2+\psi_y^2+\psi_z^2)^{\frac{3}{2}}.\end{aligned} \tag{49}$$

Since the curvature is used to calculate the surface tension force on the cell-face, the curvature on the cell-face is calculated by the following equation

$$\kappa_{i-\frac{1}{2},j,k} = \frac{1}{2}\left(\kappa_{i,j,k} + \kappa_{i-1,j,k}\right). \tag{50}$$

The curvature in the surface tension force model should be defined using the values on the gas-liquid interface, but the curvature calculated on the Cartesian grid using finite difference calculations contains numerical errors depending on the distance between the grid and the gas-liquid interface. Ref. [17] applied linear interpolation as in Eq. (50), when taking the average between two points across the gas-liquid interface. Ref. [22] proposed a curvature interpolation techniques in which the curvature on the cell-face is approximated by that on the nearest interface. Ref. [23] interpolates the curvature computed on the gas-liquid interface by an iterative process of weighted averaging that is highly sensitive to the effects on the gas-liquid interface to compute points away from the interface. In this study, the above method was tried, but it failed to reproduce the damped oscillations in the droplet oscillation problem, so a simple average as in Eq. (50) was adopted.

This is a blank page.